Journal of Geophysical Research: Oceans

RESEARCH ARTICLE
10.1029/2018JC014130

Wind Limits on Rain Layers and Diurnal Warm Layers

Elizabeth J. Thompson[1], James N. Moum[2], Christopher W. Fairall[3], and Steven A. Rutledge[4]

[1]Applied Physics Laboratory, University of Washington, Seattle, WA, USA, [2]College of Earth, Ocean, and Atmospheric Sciences, Oregon State University, Corvallis, OR, USA, [3]NOAA/Earth Systems Research Laboratory, Boulder, CO, USA, [4]Department of Atmospheric Science, Colorado State University, Fort Collins, CO, USA

Key Points:
- Rain layers were detected at values of U_{10} up to 9.8 m s^{-1}, while diurnal warm layers were only detected at $U_{10} < 7.6$ m s^{-1} (99th percentile values)
- The formation and persistence of stable layers at depths ≤ 5 m were well estimated by U_{10} and the surface buoyancy flux, B
- Rain layers (and their combinations with diurnal warm layers) formed often in disturbed and active MJO periods before westerly wind bursts

Correspondence to:
E. J. Thompson,
eliz@apl.uw.edu

Citation:
Thompson, E. J., Moum, J. N., Fairall, C. W., & Rutledge, S. A. (2019). Wind limits on rain layers and diurnal warm layers. *Journal of Geophysical Research: Oceans*, *124*, 897–924. https://doi.org/10.1029/2018JC014130

Received 3 MAY 2018
Accepted 22 OCT 2018
Accepted article online 26 OCT 2018
Published online 7 FEB 2019

Abstract Stratification of the upper few meters of the ocean limits the penetration depth of wind mixing and the vertical distribution of atmospheric fluxes. Significant density stratification at depths ≤ 5 m was observed in 38% of a 2-month data set from the central Indian Ocean collected during the DYNAMO experiment (Dynamics of the MJO, Madden-Julian Oscillation). Diurnal warm layers (DWLs) formed by solar heating populated 30% of the data set and rain layers (RLs) populated 16%. Combined contributions from rain and insolation formed RL-DWLs in 9% of the data set. RLs were detected at values of U_{10} up to 9.8 m s^{-1}, while DWLs were only detected at $U_{10} < 7.6$ m s^{-1} (99th percentile values), symptomatic of the greater buoyancy flux provided by moderate to high rain rate compared to insolation. From the ocean friction velocity, u_{*w}, and surface buoyancy flux, B, we derived estimates of $\widehat{h}_S$, stable layer depth, and $\widehat{U}_S$, the maximum U_{10} for which stratification should persist at $\widehat{h}_S$ for fixed B. These estimates predicted (1) 36 out of 44 observed stratification events (88% success rate) and (2) the wind limits of these events, which are considered to be the 99th percentile values of U_{10}). This suggests a means to determine the presence of ocean stable layers at depths ≤ 5 m from U_{10} and B. Near-surface stratification varied throughout two Madden-Julian Oscillation (MJO) cycles. In suppressed MJO periods, ($U_{10} \leq 8$ m s^{-1} with strong insolation), RLs and RL-DWLs were rare while DWLs occurred daily. During disturbed and active MJO periods, ($U_{10} \leq 8$ m s^{-1} with increased rain and cloudiness), multiple RLs and RL-DWLs formed per day and DWLs became less common. When westerly wind bursts occurred, ($U_{10} = 7$–17 m s^{-1} with steady rain), RLs formed infrequently and DWLs were not detected.

Plain Language Summary We found that rainfall and clear skies often led to stabilization of the upper 5 m of the central Indian Ocean, except during strong winds. Near-surface stable layers impact the density and mixing of the ocean because rain water and near-surface water heated by the Sun are lighter than typical ocean water, which is relatively cooler and saltier. Stable layers are important to understand because they influence sea surface temperature and ocean heat content, which impact weather and climate. Compared to previous studies, we more precisely determined the wind speed below which stable layers form and above which they do not. This will hopefully aid researchers and forecasters tasked with predicting tropical weather, climate, and ocean processes. Prior to this study, it was unclear how often ocean stable layers formed during each phase of the Madden-Julian Oscillation (MJO), a major tropical phenomenon that impacts weather and climate around the world. We found that rain layers (and their combinations with diurnal warm layers) occurred most often during disturbed and active MJO periods prior to wind bursts. Diurnal warm layers tended to form in earlier stages of the MJO, in its suppressed and disturbed periods.

1. Background and Motivation

Near-surface ocean stabilization can be achieved by either heat or freshwater inputs, which suppress subsurface mixing and confine subsequent surface inputs of heat, momentum, and freshwater to a shallow near-surface layer (Anderson et al., 1996; Asher et al., 2014; Drushka et al., 2016; Fairall, Bradley, Godfrey, et al., 1996; Fairall et al., 1997, 2006; Miller, 1976; Price, 1979; Smyth et al., 1996a, 1996b; Soloviev & Lukas, 1996; Soloviev & Vershinsky, 1982; Wijesekera & Gregg, 1996; Wijesekera et al., 1999; You, 1995). Near-surface stable layers can in turn impact sea surface temperature and salinity (SST and SSS). Thermal stratification produces diurnal warm layers (DWLs), and freshwater stratification produces rain layers (RLs). RLs occur often in tropical oceans where precipitation is high and wind speeds are relatively low (Drushka et al., 2016; Lukas & Lindstrom, 1991). However, the wind limits on RLs and the prevalence of RLs throughout the life cycle of the Madden-Julian Oscillation (MJO) are unreported. On 30- to 60-day time scales, the MJO explains the majority

of variance in tropical net heat flux, wind, SST, and rainfall (de Szoeke et al., 2014; DeMott et al., 2015; Lau & Waliser, 2005; Zhang, 2005). In contrast to RLs, numerous previous studies report on DWL persistence and DWL occurrence relative to MJO phase (Asher et al., 2014; Bellenger & Duvel, 2009; Kawai & Wada, 2007; Matthews et al., 2014; Price et al., 1986; Soloviev & Lukas, 2006; Webster et al., 1996). DWLs form in response to absorption of shortwave solar radiation within the upper few meters of the ocean. They have been observed when the 10-m level reference wind speed corrected for neutrally buoyant conditions, U_{10}, $\leq$7 m s^{-1}. The suppressed MJO period is characterized by conditions of strong solar insolation and low wind speed, so DWLs are frequently observed to form during this time. Unlike DWLs, the degree to which RLs and RL-DWL combinations can withstand turbulent mixing by wind, and their resulting occurrence throughout the MJO, remains unclear (Brainerd & Gregg, 1995, 1997; Lombardo & Gregg, 1989; Price et al., 1986).

Understanding the role of wind-forced mixing in the formation and evolution of RLs, DWLs, and RL-DWL combinations is important for predicting SST. When DWLs and RLs are present, surface inputs of momentum, heat, and freshwater are confined to shallow near-surface layers. Daytime SST anomalies in DWLs can reach at least 4 °C according to previous studies (Bellenger & Duvel, 2009; DeMott et al., 2015; Drushka et al., 2012; Fairall, Bradley, Godfrey, et al., 1996; Lau & Waliser, 2005; Matthews et al., 2014; Reverdin et al., 2012; Seo et al., 2014; Soloviev & Lukas 1997; Soloviev & Lukas, 2006; Ward 2006; Wijesekera et al., 1999; Woolnough et al., 2000). In comparison, the intraseasonal variation in daily-mean SST is typically only 1 °C (Demott et al., 2015; Lau & Waliser, 2005).

The demonstrated impact of stable layers on SST is relevant to air-sea interaction and atmospheric convection. SST impacts the latent, sensible, and radiative heat fluxes and the buoyancy flux into the atmosphere. These fluxes affect atmospheric boundary layer circulation by generating buoyant convective motion and subsequent air-pressure adjustments (Back & Bretherton, 2009a, 2009b; Bellenger et al., 2010; Clayson & Bogdanoff, 2013; Costa et al., 2001; de Szoeke et al., 2014; Fairall, Bradley, Godfrey, et al., 1996; Johnson & Ciesielski, 2017; Lindzen & Nigam, 1987; Ruppert & Johnson, 2015, 2016; Seo et al., 2014; Soloviev & Lukas, 1997; Woolnough et al., 2000, 2001). Lateral SST gradients also lead to the initiation and invigoration of precipitation due to air-pressure adjustments and low-level horizontal convergence (Carbone & Li, 2015; Li & Carbone, 2012).

Due to the impact of SST on atmospheric convection, both free-running and hindcast general circulation models produce improved MJO simulations when air-sea coupling is included in more detail, for example, with hourly-averaged surface heat fluxes using a one- or three- dimensional ocean model (Bernie et al., 2005, 2007, 2008; Chen et al., 2015; DeMott et al., 2014, 2015, 2016; Klingaman et al., 2011; Klingaman & Woolnough, 2014; Seo et al., 2014; Stan et al., 2010, and references therein). Improved MJO fidelity in general circulation models improves accuracy in predicting global weather and climate (Hung et al., 2013; Lin et al., 2006; Zhang, 2013).

Parameterizations of ocean surface stratification by rain and diurnal warming are necessary in coupled models concerned with accurate prediction of SSS and SST. DWL parameterizations and 1-D ocean mixing models can reproduce observations of ocean thermohaline structure when horizontal advection, underlying barrier layers, and other vertical processes are not dominant factors (Fairall, Bradley, Godfrey, et al., 1996; Fairall, Bradley, Rogers, et al., 1996; Price et al., 1986). For example, the Rain Impact Model (RIM) provides a macroscale (i.e., 100 km) parameterization of rain's impact on the ocean. However, RIM still requires testing with finer-scale observations of in situ U_{10} and rain rate, R (Santos-Garcia et al., 2014) and so far does not include DWLs.

Despite the importance of stably stratified surface layers in controlling SST, near-surface ocean stratification is not routinely observed. Owing to their shallow depth (typically less than a few meters), DWLs and RLs are not detected by moorings without sensors in the upper 2 m (Prytherch et al., 2013). Similarly, Argo floats, expendable bathythermograph, and many ship-based measurements often do not provide data within the first few meters of the ocean surface and provide limited temporal and spatial coverage (Anderson & Riser, 2014; Asher et al., 2014; Chi et al., 2014). Therefore, mixed layer depth climatologies developed using these data describe the regional, monthly, nighttime, or daily-mean mixed layer depth, which is typically 10–30 m in the central Indian Ocean and varies by ±15 m throughout an MJO cycle (de Boyer Montegut et al., 2004, DeMott et al., 2015; Drushka et al., 2012; Holte et al., 2017; Schmidtko et al., 2013). Climatologies developed using Argo data focus on mixed layer depth variability over time scales on the order of 1 to 2 days since Argo data do not sample fast enough nor with sufficient vertical resolution near the sea surface to resolve diurnal or subdiurnal processes in the upper 10 m.

Both Argo profiles and satellite overpasses are too infrequent relative to rain events to characterize the occurrence rate of RLs and RL-DWLs or to determine their sensitivity to U_{10}. To some extent, the presence of RLs and DWLs can be detected by comparing the uppermost Argo or mooring measurements of S and T with satellite-derived SSS or SST (Anderson & Riser, 2014; Boutin et al., 2013; Drushka et al., 2016; Kawai & Wada, 2007). However, scatterometer- and radiometer-based measurements of U_{10}, SSS, and SST are contaminated by precipitation and their 25- to 100-km scale footprints can also be too coarse spatially and temporally (e.g., updating only a few times per day) to resolve the atmospheric mesoscale footprint of rain (Kilpatrick & Xie, 2015, 2016; Kummerow et al., 1998).

Ship observations have detected stable near-surface salinity gradients generated by rain for a range of rain rates so long as $U_{10} < 9.5$ m s^{-1} (Anderson et al., 1996; Asher et al., 2014; Cronin & McPhaden, 1999; Smyth et al., 1996a, 1996b; Soloviev & Lukas 1997; Wijesekera & Gregg, 1996; Wijesekera et al., 1999; You, 1995). In contrast, observations during tropical storms ($U_{10} \geq 18$ m s^{-1}) and hurricanes ($U_{10} \geq 33$ m s^{-1}) do not show the presence of stably stratified RLs (D'Asaro et al., 2014; Jourdain et al., 2013). From these previous studies, it remains unclear whether 9.5 m s^{-1} represents the upper limit of U_{10} at which a RL can form, and if indeed this value is an upper limit, why that should be the case. According to these previous studies based on field measurements, understanding the formation and evolution of RLs, including the effect of wind speed on their lifetime, is complicated by several factors:

1. in addition to local rain, freshwater from nearby rain can be advected by the current into ocean sensors;
2. RLs spread and propagate laterally like density currents (Soloviev et al., 2015); and
3. RL creation and longevity depend on upper ocean turbulence and mixing driven by wind and waves.

These factors explain why RL observations are not always highly correlated to their generating rain events and why RL detection is not guaranteed from every rain event even if near-surface salinity measurements are available, as noted by You (1995). Observations (Asher et al., 2014) and model results (Drushka et al., 2016) suggest that shallow, stable near-surface vertical salinity gradients generated by rain form primarily when the rain rate, R, ≥ 5 mm h^{-1}. For tropical ocean conditions, the buoyancy produced by $R = 5$ mm h^{-1} is equal and opposite to the buoyancy destroyed by a surface cooling on the order of $Q_{Net} = 400$ W m^{-2} (demonstrated in Appendix A, also see Dorrestein, 1979). Additional turbulence may also be provided by wind, waves, or subsurface shear. Thus, when $R < 5$ mm h^{-1}, the freshwater from rain tends to be mixed into the water column by a combination of surface cooling and turbulent mixing so that a stratified surface fresh layer does not form. Miller (1976) also modeled RLs, noting that initializing light rain rates with strong winds (45 mm accumulation over 15 hr while $U_{10} = 10$ m s^{-1}) resulted in the formation of a mixed layer that was 38-m deep with no detectable SSS or SST change. This showed that the rain was mixed downward and formed a homogeneous layer. When high rain rates were modeled with low wind speeds (45 mm accumulation over 4 hr while $U_{10} = 5$ m s^{-1}), a RL formed at 0.76-m depth and the greatest changes in SST and SSS were observed.

Our current understanding of RLs motivates the following questions:

1. What is the maximum U_{10} under which a RL or RL-DWL can form and persist?
2. Is this upper limit of U_{10} a function of R?
3. How often do RLs and RL-DWL combinations occur throughout the suppressed, disturbed, active, and westerly wind burst (WWB) periods of the MJO?

The ocean surface buoyancy flux and the turbulent kinetic energy (TKE) input to the ocean provided by wind are both functions of MJO phase (e.g., Moum et al., 2014; Zhang, 2005). This should impact the formation and persistence of surface stratification throughout the MJO life cycle. The penetration depth of wind mixing into the ocean is determined by a balance between stabilizing buoyancy forces and TKE production as given by Monin-Obukhov theory (Brainerd & Gregg, 1995, 1997; Lombardo & Gregg, 1989; Price et al., 1986). This theory suggests that a near-surface stable layer can persist during high wind speeds, provided the stabilizing buoyancy flux is large enough. If this hypothesis is true, then RL and RL-DWL formation should be most likely in disturbed and active MJO periods when high rain rates occur, even though surface wind speed may be great at times (e.g., de Szoeke et al., 2014, 2017; Zhang, 2005). In the western Pacific warm pool, RL formation was observed during a WWB with prolonged rain and $U_{10} = 9.5$ m s^{-1} (Wijesekera et al., 1999). This indicates that RL formation is possible during WWBs despite strong winds. In contrast to RLs, DWLs have typically only been observed during the suppressed phase of the MJO and

when $U_{10} \leq 6$–7 m s^{-1} (Bellenger & Duvel 2009; Matthews et al., 2014; Webster et al., 1996). As will be shown in this study, the buoyancy created by rain is typically an order of magnitude greater than that due to peak net surface heating. Therefore, it stands to reason that RLs should form and persist at higher U_{10} than DWLs, and RLs should also occur in disturbed and active stages of the MJO, after the suppressed MJO period that is characterized by frequent DWLs.

This study makes use of ship-based surface observations, including measurements of air-sea fluxes, radar-observed rain, and in situ vertical profiles of ocean salinity and temperature. These data are used to better understand how wind stress interacts with the buoyancy flux in the formation and evolution of DWLs, RLs, and RL-DWLs observed throughout the MJO life cycle. The data used were collected in the central Indian Ocean throughout the two MJO cycles observed during the 2011 Dynamics of the MJO (DYNAMO) experiment (Johnson & Ciesielski, 2013; Moum et al., 2014; Yoneyama et al., 2013). A method is developed for identifying the presence of a near-surface ocean stable layer. This method is used to track ocean stratification from the combined effects of diurnal warming and rain and to explore the sensitivity of stable layer formation and persistence to U_{10}. Observations are compared to estimates of stable layer depth and stable layer wind limits that were derived from Monin-Obukhov similarity theory.

2. Observations and Analysis Methods

2.1. Field Program and MJO Time Periods

Here we examine 42 days of DYNAMO observations made from the research vessel (R/V) *Roger Revelle* at 0°N and 80.5°E (Johnson & Ciesielski, 2013, Moum et al., 2014, Yoneyama et al., 2013). We examined times when precipitation radar, upper ocean, and surface data were all available: from 5 October to 28 October and 12 November to 29 November 2011. These two time periods are separated by a 15-day restaffing, refueling, and transit period.

Four time periods of the MJO were identified for this study region using the Real-time Multivariate MJO (RMM) index (Table 1, http://monitor.cicsnc.org/mjo/curent/rmm/). The RMM index describes MJO conditions by combining tropical atmospheric measurements of outgoing longwave radiation (i.e., cloudiness) and zonal winds at 850 and 200 mb (Wheeler & Hendon, 2004). Previous studies have used the RMM index for guidance in describing the state of the MJO (e.g., Gottschalck et al., 2013; Johnson & Ciesielski, 2013; Lau & Waliser, 2005; Rowe & Houze, 2015; Xu & Rutledge, 2014, 2015; Zhang, 2005). Phases 4–7 of the RMM index were not well observed in the central equatorial Indian Ocean during DYNAMO. We concentrate here on four specific periods, described in terms of atmospheric forcing conditions as *suppressed* (RMM phases 7 and 8), *disturbed* (phase 1), *active* (phases 2 and 3) and *WWB* (representing phase 3 when $U_{10} > 7$ m s^{-1} for at least 1 day; westerly wind burst criterion defined by Harrison & Vecchi, 1997). Statistics associated with each of these four periods are documented in Table 1. These time periods were used by Pujiana et al. (2018). The 42 total observation days in this study are made up of 14, 12, 10, and 6 days in the suppressed, disturbed, active, and WWB periods (Table 1).

In the central Indian Ocean, the suppressed MJO period is observed during RMM phases 5–8. Excluding the beginning of phase 5, these days typically have weak winds along with infrequent clouds and rain. DYNAMO days with upper ocean observations did not coincide with phases 5 and 6, so suppressed MJO days in this study only spanned phases 7 and 8. In November 2011, phase 7 only lasted three total days and observations were only collected on the last day; however, observations were collected during all 4 days of phase 8 in this month. In October 2011, data were collected on all 10 days of phases 7 and 8. The suppressed period in this study is identical to that defined by Ruppert and Johnson (2015, 2016) and to the *undisturbed period* used by Johnson and Ciesielski (2017).

During the disturbed MJO period (RMM phase 1), clouds and precipitation become more frequent, more intense, and more expansive in terms of area (e.g., Riley et al., 2011; Xu & Rutledge, 2014). The disturbed period begins on the day when the RMM index first equals 1; this day is regarded as the onset of the MJO by Ruppert and Johnson (2015, 2016) and Johnson and Ciesielski (2017). These previous studies define a disturbed period that spans all days following the onset of the MJO, so the beginning of the disturbed period is the same in these studies and the current study. DYNAMO observations were made on all 12 days of RMM phase 1 that occurred over both months.

Table 1
Meteorological Conditions During Two MJOs Observed During This DYNAMO Data Set

	MJO time period				
	Suppressed (14 days)	Disturbed (12 days)	Active (10 days)	Westerly wind burst (WWB, 6 days)	Total (42 days)
RMM index	7[a]–8	1	2–3[a]	2–3 when $U_{10} > 7$ m s^{-1}	1–8[a]
Time sampled while *Revelle* at 80.5°E, 0°	05–14 Oct 12–17 Nov	14–20[%] Oct 17–21[%] Nov	20[%]–27[@] Oct 21[%]–24[#] Nov 27–27[$] Nov	27[@]–28 Oct 24[#]–27 Nov 27[$]–29 Nov	05–28 Oct 12–29 Nov
Max R (mm h^{-1})	19	65	74	69	74
Mean R (mm h^{-1})	0.03	0.28	0.51	1.45	0.42
99th percentile value of U_{10} (m s^{-1})	7.9	8.1	9.1	15.9	13.1
Mean U_{10} (m s^{-1})	4.1	2.7	4.1	9.1	4.3
Median of daytime peak (minimum) Q_{Net} (W m^{-2})	−853	−886	−847	−523	−855
Mean of daytime Q_{Net} (W m^{-2})	−446	−366	−249	3	−323

Note. MJO conditions at R/V *Revelle* location (80.5°E, 0°) according to Wheeler and Hendon (2004) RMM index (http://www.bom.gov.au/climate/mjo/graphics/rmm.74toRealtime.txt). Time periods defined in this study start or end at 00Z except when denoted by superscript # = 08Z; @ = 10Z; $ = 17Z; % = 22Z. Two WWB pulses occurred during the November active MJO phase. Mean rain rate and wind speed are calculated from *Revelle* gauge measurements. Sign convention for net heat flux is negative into the ocean (heating the ocean). Daytime hours were considered to be 7 a.m. to 5 p.m. LST, 1–11 UTC.
[a]The DYNAMO time periods in which complete vertical profiles of the ocean were measured at *Revelle* did not span all phases of the RMM index. Observation days did not include phases 4, 5, or 6. Observations were also not collected on all days of phases 7 or 3 (see section 2.1 for details)

On active MJO days (RMM phases 2 and 3), rain and clouds persisted throughout a majority of the daytime and nighttime hours, values of 24-hr rain accumulation and precipitation size reached maximum values, and stratiform rain contributed greatly to total rain amounts (determined with shipborne radar data by Xu & Rutledge, 2015). All 10 days of these active MJO conditions were observed during DYNAMO.

According to the definition by Harrison and Vecchi (1997), the WWB time period occurred in the DYNAMO study region on days when the RMM index was 3–4 and when $U_{10} > 7$ m s^{-1} for more than 1 day. During this period, rain was widespread, long lasting, and made up of both convective and stratiform components, (e.g., Moum et al., 2014; Xu & Rutledge, 2015). DYNAMO ocean observations were not collected during phase 4, but 1 and 5 days of WWB conditions in phase 3 were observed in October and November, respectively.

2.2. Surface Meteorology and Air-Sea Fluxes

Near-surface meteorology (air temperature, specific humidity, wind speed, and wind direction at nominally 10 m above the sea surface) and air-sea flux estimates are at ftp://dynamo.dms.uconn.edu/ linked by the Earth Observing Laboratory field catalog: http://data.eol.ucar.edu/master_list/?project=DYNAMO. Air-sea fluxes were computed using the COARE (Coupled Ocean-Atmosphere Response Experiment) version 3.5 bulk aerodynamic algorithm (Fairall et al., 1997, 2003; Fairall, Bradley, Rogers, et al., 1996; Edson et al., 2013, see complete description for DYNAMO experiment in de Szoeke et al., 2014). These data are available at 1- and 10-min resolution. The 10-min flux and surface data were utilized to match 10-min resolution precipitation radar data and interpolated ocean data. A 10-min resolution time series of R from the ship was acquired by resampling the 1-min instantaneous R data from ship gauges without performing any temporal smoothing. The net heat flux, Q_{Net}, was defined negative downward into the ocean (heating the ocean) and positive upward out of the ocean (cooling the ocean).

2.3. Precipitation

Data from the National Aeronautics and Space Administration Tropical Ocean-Global Atmosphere (NASA TOGA) C-band Doppler radar on the R/V *Revelle* are also found on the Earth Observing Laboratory field catalog (http://data.eol.ucar.edu/master_list/?project=DYNAMO). These were quality controlled to remove second trip echo and sea clutter and to correct for attenuation (details in Xu & Rutledge, 2014). Polar-coordinate data were gridded using RadX2Grid, provided by the National Center for Atmospheric Research (https://www.ral.ucar.edu/projects/titan/docs/radial_formats/radx.html), to a 0.5-km horizontal, 0.75-km vertical Cartesian grid within 25-km range of the ship. Coarser 2-km horizontal resolution gridded data were also investigated out to the full range of the radar, 150 km, but are not presented herein. Radar data were at 10-min resolution. The radar's *cone of silence* limited the first usable radar data to 2-km range.

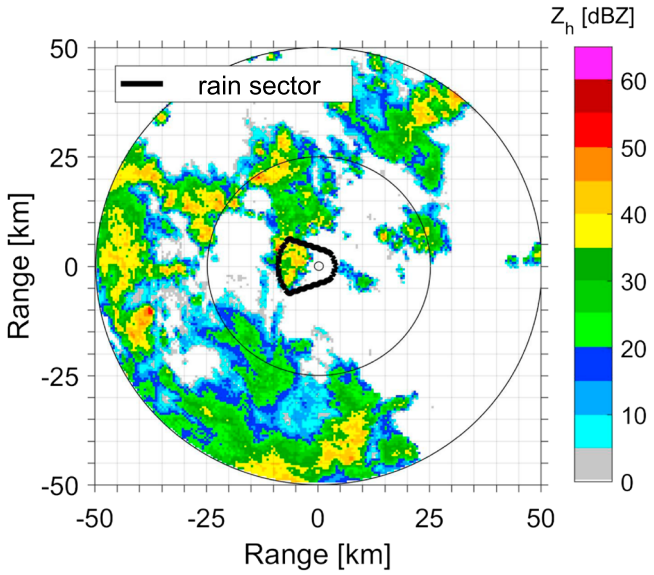

Figure 1. R/V *Revelle* (0°, 80.5°E, position denoted by center circle) radar reflectivity (Z_h) with outline of rain sector area (thick black line). The sector extends 9 km from *Revelle* in the upstream direction and extends 4 km from *Revelle* in all other directions. The upstream extension of the sector accounts for surface advection of rain water within approximately the last 3 hr by the mean 0.8 m s^{-1} eastward current that existed during these cruises.

Radar reflectivity, Z_h, was partitioned into convective and stratiform rain areas using the algorithm by Yuter and Houze (1998). Then R was estimated in each area with either a convective or stratiform equation for $R(Z_h)$, which were fitted to account for tropical oceanic rain variability by Thompson et al. (2015). Separate convective and stratiform R (Z_h) equations help reduce error in R estimation compared to treating the entire Z_h field with a single R (Z_h) equation fit to all data (Thompson et al., 2015). More details about these radar data procedures are in Appendix B.

Radar data were queried to identify times when precipitation existed upstream of the research ship. The research ship was always directed westward into the eastward flowing surface current, which was typically 0.8 m s^{-1}. A rain sector area was defined to extend 9 km from the ship in the upstream direction, from 235° to 300°, and to extend 4 km away from the ship in all other directions (Figure 1**,** 104 km^2 total sector area). Sector extensions of 9 and 15 km were tested, which corresponded to advective time scales of about 3 hr and 4.5 hr from the upstream edge of the sector to the ship. Upper ocean evolution related better to rain within the sector that extended only 9 km upstream, so this extension distance was chosen for the rest of this study.

Values of R from the ship radar's rain sector and from the ship's gauge were combined to form a 10-min resolution time series of R_{MAX}, the maximum R sampled from either the ship gauge or within the radar sector. Using this time series of R_{MAX}, 68 periods of rain were identified over the course of 42 intensive observation days. In order to qualify as a new rain event, rain was required to have not occurred for the previous 30 min. Rain event classification did not involve a minimum duration threshold, so the shortest rain event was the same resolution as the data set, 10 min.

2.4. Ocean T and S

SST and bulk near-surface values of temperature, T, and salinity, S, were provided in the flux data set discussed in section 2.2. SST was measured at roughly 0.05-m depth by a sea snake, a towed thermistor contained within a brass body that was sealed inside a floating Tygon tube (Fairall, Bradley, Godfrey, et al., 1996a). Bulk T and S were measured by the ship's thermosalinograph using an intake at 5-m depth at the bow of the ship. The Chameleon profiler (Moum et al., 1995) was deployed from the stern of the ship and provided vertical profiles of S and T at 7-min intervals with 1-m vertical resolution between 350-m depth and the sea surface depending on waves and swell. Near-surface water was mixed by the ship's wake, so useful measurements began at 2- to 3-m depth. Ten thermistors sampling T at least 20 times per minute were also tethered along a chain at a distance of 5 m away from the starboard bow. The thermistors were unequally spaced between depths of 1.5 m $\leq z \leq$ 7.5 m along the chain (z is the vertical coordinate, $z > 0$ downward). The vertical positions of the thermistors varied by approximately 0.5–1.0 m depending on the speed of the ship, the surface current, and surface gravity waves. These data were interpolated to a 1-m vertical grid. When the ship was headed into a steady mean eastward surface current, the thermistor chain provided a record of T measurements undisturbed by the ship's wake (Moulin et al., 2018). In comparison, Chameleon profiling from the stern as the ship remained stationary and pointed into the steady eastward current. This approach yielded vertical profiles of T and S that were disturbed by the ship's propulsion system over $z < 7$ m (the draft of *Revelle* is 5 m). In order to assemble vertical profiles of T and S that were most representative of open-ocean conditions, sea snake SST data and thermistor chain T data were used at $z < 5$ m, thermistor chain and Chameleon T data were averaged at $z = 5$ m and $z = 6$ m, and Chameleon T data were used at $z > 7$ m. Chameleon profiles provided the shallowest and most temporally continuous set of S measurements, which were used exclusively for S vertical profiles in this study. These vertical profiles of ocean T and S were resampled to the 10-min interval of radar and flux data sets without performing any temporal smoothing, meaning that data points closest in time to the 10-min interval were used.

2.5. Ocean Stability

Vertical T and S gradients were used to calculate N^2, the Brünt-Vaisala frequency. The value of N is a measure of static stability and relates to the natural frequency of internal gravity waves:

$$N^2 = \frac{g}{\sigma}\frac{\mathrm{d}\sigma}{\mathrm{d}z} \tag{1}$$

where σ is the sea water potential density. The value of N^2 is positive for a statically stable layer of water and negative for unstable conditions that are prone to convective overturning and vertical mixing. The linear approximation of the equation of state of seawater leads to an N^2 expression that can be scaled by the individual effects of S and T on σ:

$$N^2 \cong N^2_{S+T} \cong N^2_T + N^2_S \tag{2}$$

$$N^2_T = g\alpha\frac{\mathrm{d}T}{\mathrm{d}z} \tag{3}$$

$$N^2_S = g\beta\frac{\mathrm{d}S}{\mathrm{d}z} \tag{4}$$

where α ($°C^{-1}$) is the thermal expansion coefficient of seawater:

$$\alpha = \frac{-1}{\sigma}\frac{\partial\sigma}{\partial T} \tag{5}$$

and β (PSU^{-1}) is the salt contraction coefficient of seawater:

$$\beta = \frac{1}{\sigma}\frac{\partial\sigma}{\partial S} \tag{6}$$

Signs in (5) and (6) reflect that density increases as water becomes colder and saltier, such that (3) and (4) describe how the water column becomes more stable when a lighter fluid sits atop a denser fluid. The α and β coefficients were calculated using the Gibbs-SeaWater Oceanographic Toolbox (McDougall & Barker, 2011) for each time and depth pair of S and T measurements during DYNAMO. Then, N^2_S and N^2_T were calculated between each vertical level at each time interval using estimated α and β and the measured vertical S and T gradients. Fields of N^2 were smoothed with a 3-m vertical running mean filter with 1-1-1 weighting. Vertical profiles of N^2_{S+T} calculated with (2) were nearly equivalent to vertical profiles of N^2 calculated directly from the vertical density gradient in (1). Therefore, N^2_{S+T} from (2) is used throughout this study and is abbreviated henceforth as N^2. Estimates of N^2_S were available starting at 2–3 m, while estimates of N^2_T were available from 0 to 350 m. Therefore, N^2 was determined solely by N^2_T where $z < 2$ m.

2.6. Ocean Stable Layer Identification Algorithm

Depth ranges were considered well mixed if $-4.5 \times 10^{-5} < N^2 < 4.5 \times 10^{-5}$ s^{-2} over at least three consecutive meters vertically. Water was considered stable if $N^2 > 4.5 \times 10^{-5}$ s^{-2} for at least two consecutive meters vertically. Using these definitions, an algorithm was devised to search for the top of the shallowest stable level in the ocean column, h_S, at 10-min intervals. In this manuscript, the top depth of the stable layer is often referred to simply as the stable layer depth (they are considered to be equivalent). The stable layer top depth and the stable layer depth are used interchangeably to refer to hS in this manuscript. The algorithm also determined the base of the shallowest stable layer, h_B. Stable layers were required to be at least 2 m in vertical thickness in this study because data with 1-m vertical resolution were used. Therefore, the minimum stable layer thickness in this study was 2 m (i.e., $h_B - h_S \geq 2$ m). The minimum depth of h_S was 0 m. The top depth of the thermocline, h_{TC}, was defined as the first level over which $N^2 > 1.75 \times 10^{-4}$ s^{-2} for at least three consecutive meters. The top depth of the thermocline and the thermocline depth are considered equivalent and used interchangeably. If the algorithm could not identify a stable layer shallower than 45 m or within 10 m of h_{TC}, the ocean was considered to be well mixed from the surface to the thermocline and h_S was reassigned to

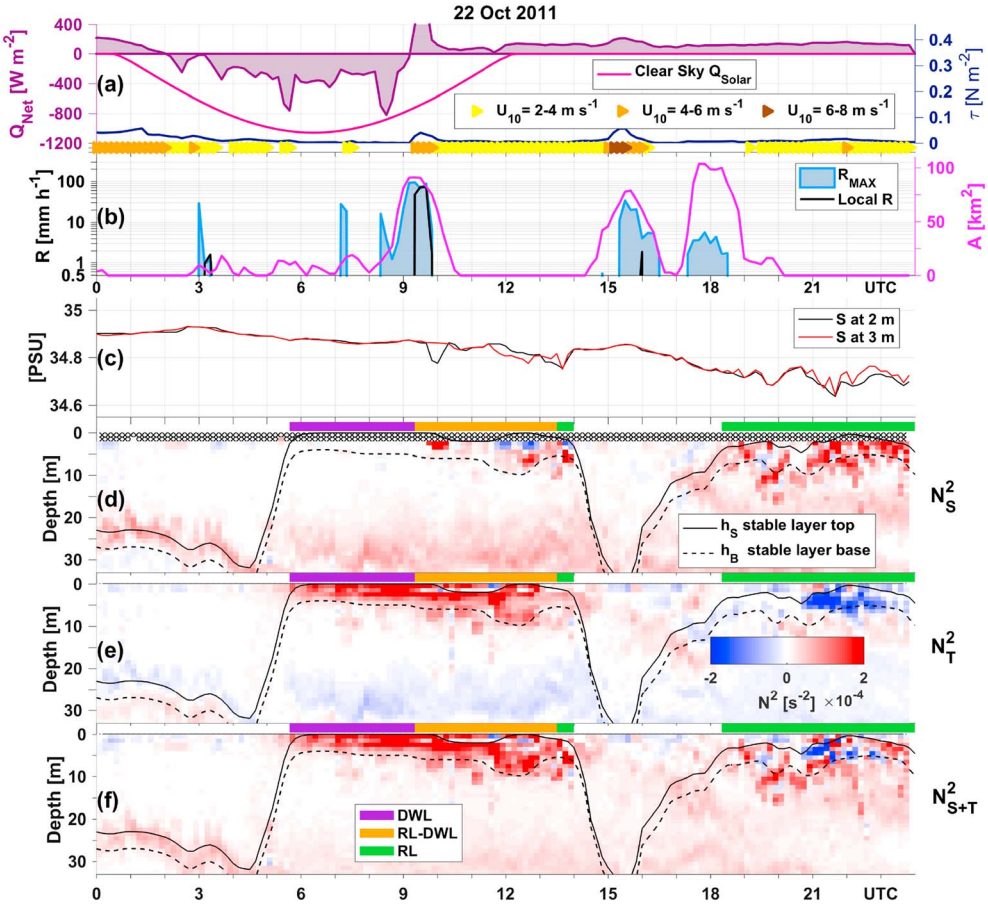

Figure 2. The 22 October 2011 case study of a DWL, a RL, and a RL-DWL combination (colored bars on top of (d–f)): (a) net heat flux, Q_{Net}, modeled solar heat flux for clear-sky conditions, Q_{Solar}, wind stress, τ, and triangles color-coded by U_{10}; (b) rain rate observed locally at the research ship (R) and the max value observed either locally or within the upstream radar sector, R_{MAX}, and the area, A, of the radar sector that was filled by rain echoes; (c) S at 2- and 3-m depth from Chameleon profiler; (d) N^2_S; (e) N^2_T; (f) N^2_{S+T}. Solid and dashed lines in Figures 2d–2f indicate the depth of the stable layer top, h_S, and the depth of the stable layer base, h_B. DWL = diurnal warm layer; RL = rain layer.

h_{TC}. In this case, the shallowest stable layer was the thermocline and $h_S = h_{TC}$. These thresholds and methodology were manually tested until the algorithm yielded physically consistent results across all 42 days of analysis. After these rules were applied, h_S, h_B, and h_{TC} were smoothed with a running 50-min filter with 1-1-2-1-1 weighting.

The quantities $\overline{N^2_S}$ and $\overline{N^2_T}$ were determined by vertically averaging the N^2_S and N^2_T fields between 0 and 5 m and then smoothing the resulting time series with a running 30-min filter with 1-2-1 weighting. RLs and DWLs were defined to begin when $\overline{N^2_S}$ and $\overline{N^2_T} > 1.5 \times 10^{-5}$ s^{-2}, respectively, and $h_S \leq 5$ m. Not all DWLs or RLs were associated with the creation of a new stable layer or with h_S shoaling because near-surface stratification with respect to the other state variable (S or T) could have already existed. RL and DWL events were determined to end when $\overline{N^2_S}$ and $\overline{N^2_T} < 1 \times 10^{-7}$ s^{-2}, respectively, or when $h_S > 5$ m, whichever event occurred first. To be classified, RL and DWL events were required to last at least three consecutive observations (spanning 30 total minutes) and be at least 1 hr apart from stable layers of the same type. Therefore, a RL could form in close succession to a DWL, but, in order to be classified as an individual event, the RL must be at least 1 hr away from the next or previously identified RL.

Bow N^2_T profiles extended to the surface, whereas stern N^2_S profiles began at 2–3 m. The bow N^2_T profiles did not suggest that cold, fresh layers were deposited by rain shallower than 2 m. In other words, the N^2_T data do not suggest that RLs were missing from N^2_S profiles, although it is possible the T profiles did not capture all stratification events. Even if RLs began earlier or shallower than suggested by the S measurements from 2 to 3 m,

the stable S gradients ought to mix downward past the 2- to 3-m measurements throughout the lifetime or decay of the RL. Therefore, our record of RLs is most likely not comprehensive, but our record should be representative of the majority of RLs that occurred at this central Indian Ocean location during DYNAMO.

Our RL and DWL identification algorithm is demonstrated on a time period beginning at 00:00 UTC, 30 min prior to sunrise (Figure 2). On this day, which was classified as *active* MJO conditions, a DWL formed at 06:00 UTC (local noon) as Q_{Net} reached -300 W m^{-2} and U_{10} decreased to below 4 m s^{-1} (Figures 2a and 2d) The DWL was marked by $h_S = 0$ m owing to the strongly positive N_T^2 at $z < 5$ m (Figure 2e). Rain fell intermittently upstream of the ship during the DWL between 07:00 and 10:00 UTC, midafternoon (Figure 2b). Rain only occurred locally at the *Revelle* between 09:30 and 10:00 UTC. Contemporaneously with the local rain accumulation, N_S^2 became positive over the same depths as the DWL, making this a RL-DWL combination (Figures 2d–2f). Stratification of both S and T disappeared at 14:00 UTC (08:00 p.m.) as U_{10} increased rapidly to 6–8 m s^{-1} while Q_{Net} ~ 100–200 W m^{-2}, indicating the ocean surface was cooling (Figures 2a, 2d, 2e, 2f). Rain occurred upstream of the ship from 15:00 to 17:00 UTC (evening) while U_{10} reached 6–8 m s^{-1} (Figures 2a and 2b). There was no RL observed locally as a result of this upstream rain event (Figures 2d–2f). Instead, N_S^2 and N_T^2 indicated that the ocean was well mixed between the surface and a depth of 30 m.

Later that night at 17:00 UTC, 11:00 LST, the wind weakened ($U_{10} < 2$ m s^{-1}) and a large area of weak-to-moderate rain began upstream of the ship ($R_{MAX} = 7$ mm h^{-1}, Figures 2a and 2b). Following this series of events, N_S^2 and N_{S+T}^2 became strongly positive near the ocean surface, indicating the presence of a second RL (Figure 2d). Within this nighttime RL, N_T^2 was negative due to the combined cooling effects of rain, latent, sensible, and radiative fluxes (Figure 2e). The unstable N_T^2 within the RL due to surface cooling was not large enough magnitude to render the entire layer unstable, since N_{S+T}^2 (i.e., N^2) remained mostly positive (Figure 2f). The nighttime RL lingered at $z < 5$ m for over 6 hr after upstream rain ended (Figure 2b). The daytime RL persisted 4 hr after upstream rain ended, 5 hr after local rain ended. Both RLs were coincident with 2- and 3-m depth freshening trends and fresher 2 m S compared to 3 m S (Figure 2c), leading to stable vertical gradients of S and therefore positive N_S^2 (Figure 2d). During the DWL, RL, and RL-DWL events, $h_S \leq 5$ m and the stable layer thickness, $h_B - h_S$, was roughly 2 m (Figures 2d–2f). This daily analysis was used to test the stable layer identification algorithm on all 42 DYNAMO observation days.

3. Results

This section examines the frequency of occurrence of RLs, DWLs, and RL-DWLs observed throughout two MJO cycles during DYNAMO and the conditions in which these stable layers existed.

3.1. Stable Layer Occurrence and Depth

From our DYNAMO record, rain and surface warming both played significant roles in creating stable near-surface ocean conditions in which $h_S \leq 5$ m (Figure 3 and Table 2). In other words, over the course of 42 observation days, 44 events occurred in which one or more stable layers were present at $z \leq 5$ m: 14 DWL-only events, 14 RL-only events, and 16 events in which RLs and DWLs combined one or more times. We sampled 30 DWLs (299 observation hours, 30% of the data record) and 32 RLs (165 hr, 16% of the data record). RL-DWL combinations were almost 2 times more likely to be RLs contained within preexisting DWLs than vice versa. For example, 10 DWLs contained one or more RLs and only 6 RLs contained DWLs; 12 RLs formed on top of preexisting DWLs but only 7 DWLs formed on top of preexisting RLs. The total number of continuous stratification events in which RLs and DWLs combined was only 16 even though 18 individual RL-DWL events were observed. This is because one DWL contained 2 RLs, and another DWL formed in a preexisting RL that also later contained a new RL. RL-DWLs occupied 89 hr, or 9%, of the DYNAMO data record. RLs without DWL influence spanned only 8% of the data set, while DWLs without RL influence spanned over twice as much (21%) of the data set. Collectively, over the course of two MJOs, daytime warming and rain caused stable layers to exist at $z \leq 5$ m during 38% of the data set, and $z \leq 10$ m during 57% of the data set (Figures 3 and 4).

When RLs and DWLs were not present, water was mixed between the surface and the thermocline, meaning the shallowest ocean stable layer was the thermocline and $h_S = h_{TC}$ **(**Figure 3**).** This situation occurred during 13% of the data set. When RLs and DWLs decayed, these stable layers mixed downward to about 40-m depth

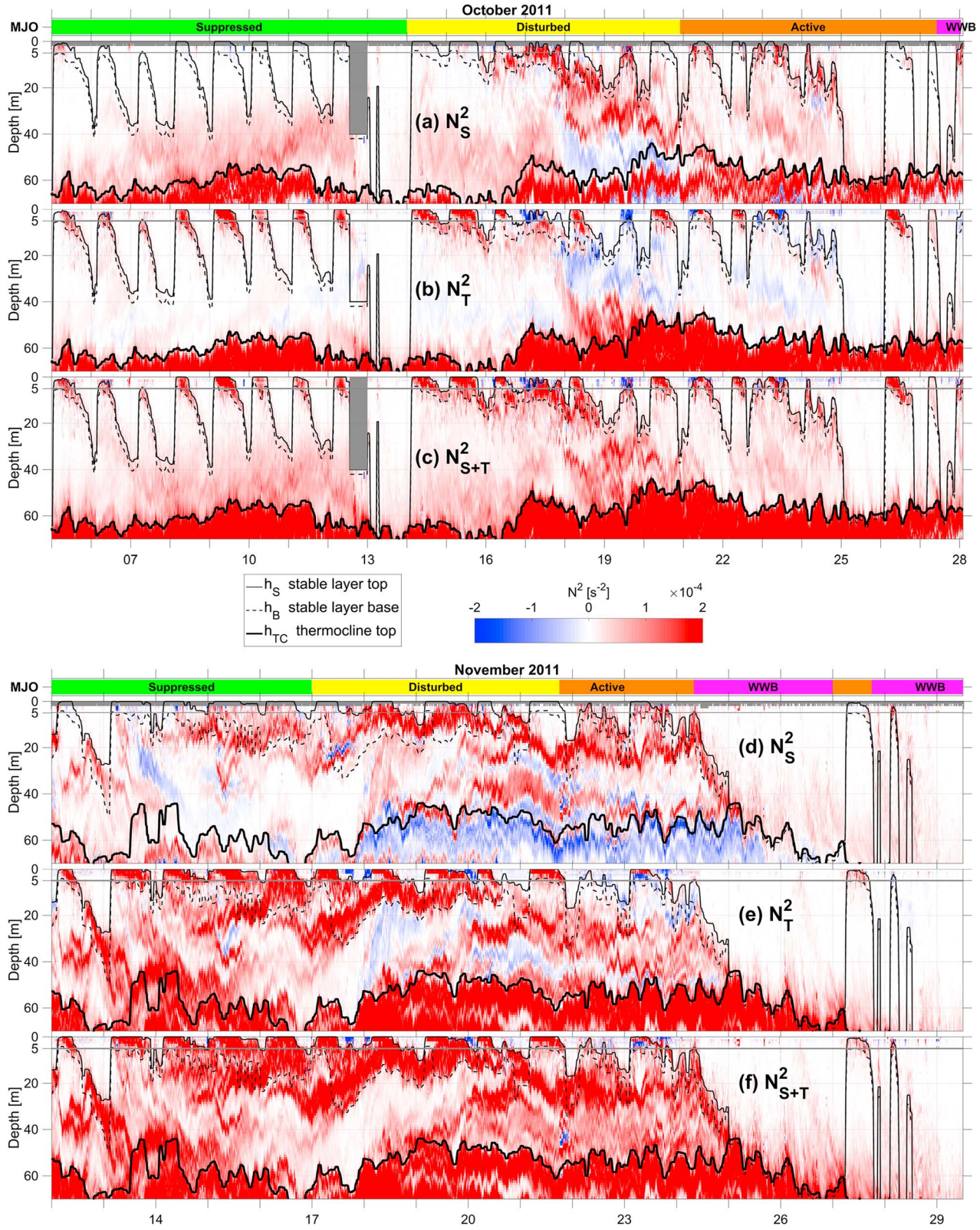

Figure 3. Observed N^2 due to S (a, d), T (b, e), both S and T (c, f) as a function of depth and time during two equatorial, central Indian Ocean cruises. The depth of the stable layer top, h_S, the stable layer base, h_B, and the thermocline top, h_{TC}, were determined by the total N^2 field (c, f). A line marks the depth of z = 5 m. The state of the MJO was defined by the RMM index (*WH04*), which corresponds to suppressed, disturbed, active, and westerly wind burst (WWB) time periods in this study (Table 1, section 2.1).

Table 2
Stable Layers Observed Throughout Two MJO Life Cycles

		MJO time period				
		Suppressed (14 days)	Disturbed (12 days)	Active (10 days)	Westerly wind burst (WWB, 6 days)	Total (42 days)
stable layer count	RL only	0	7	5	2	14
	DWL only	11	2	1	0	14
	RL-DWL combo	2	8	6	0	16
	all RLs	2	16	12	2	32
	all DWLs	13	10	7	0	30
	continuous stable layer events	13	17	12	2	44

Note. Count of observed stable layers in each MJO period defined by the RMM index (Table 1, section 2.1). The continuous stable layer event category counts events in which multiple RLs and/or DWLs were present at the same time as a single continuous event. Events in which RLs and DWLs were combined (RL-DWL) occurred 18 individual times but contributed to only 16 continuous RL-DWL events. This is because 2 RL-DWL events were contained within preexisting stable events in which another RL-DWL was also present. The total number of continuous stable layers is equal to the sum of the stable layers in RL only, DWL only, and RL-DWL categories. RL = rain layer; DWL = diurnal warm layer.

in October 2011 (days 5–13 and 21–27). In November 2011, a month during which a stable barrier layer existed between 10 and 30 m, RLs and DWLs only mixed downward to about 10-m depth (Figure 3, days 14–24). During the first November WWB pulse on 24–26 November, this barrier layer eroded and the thermocline rapidly deepened from 57m to 90 m (Figures 3 and 4c, also discussed by Moum et al., 2014 and Chi et al., 2014). Abrupt shifts in vertical T and S stability structure were noted on 18 and 24 October and 12, 14, 15, and 18 November, which appear to be the result of advection (discussed further in section 3.2 and by Chi et al., 2014).

RLs, DWLs, and RL-DWL combination stable layers were most frequently observed to be between 2- and 8-m thick, with a mean thickness of 6 m and median thickness of 4 m (Figures 3 and 4b). These thickness observations are only slightly greater than the 2- to 4-m thickness estimates from previous modeling studies (Drushka et al., 2016; Lombardo & Gregg, 1989; Lukas & Lindstrom, 1991; Miller, 1976; Price, 1979; Price et al., 1986).

While this data set's mean stable layer depth, $\overline{h_S}$, of 20 m agrees with the 18-m mean mixed layer depth estimate based on Argo profiles for this location in October–November from de Boyer Montégut et al. (2004) and also roughly with the 36-m mean depth from Holte et al. (2017), the high-resolution values of h_S from DYNAMO were only within ±5 m of $\overline{h_S}$ during 9% of the data set (Figures 3 and 4). In the other 91% of the data set, the penetration depth of wind mixing was either overestimated or underestimated by $\overline{h_S}$ by at least 20 m, which led to errors of 100% or greater. The standard deviation of h_S was 25 m, 5 m greater than $\overline{h_S}$. Thus, $\overline{h_S}$ and the mean mixed layer depths from Argo are not representative of the daily and subdaily upper ocean stabilization events observed during this experiment (Figures 3 and 4). For example, rain and diurnal heating stabilized the upper 5 m of the ocean on 37 out of 42 observation days, while waters were well mixed between the surface and 40- to 60-m depth on 20 out of 42 days. Instances of $h_S = 20$ m (i.e., $h_S = \overline{h_S}$) were brief, occurring only as near-surface stable layers were forming, deepening, or decaying.

3.2. Wind Limits of Stable Layers

The 99th percentile value of U_{10} observed in the presence of stable layers was 9.8 m s^{-1} for RLs, 7.6 m s^{-1} for DWLs, and 5.5 m s^{-1} for RL-DWLs. These values are considered to be the wind limits on each type of stable layer. Very few instances occurred in which RLs were present and $U_{10} > 10$ m s^{-1} (9 data points) or in which DWLs were present and $U_{10} > 7$ m s^{-1} (27 data points total, Figure 5). The overall highest value of U_{10} observed during a RL was 11.3 m s^{-1}, compared to 9.2 m s^{-1} in a DWL and 6.3 m s^{-1} in RL-DWLs (Figure 5). Numerous previous studies have also found that DWLs are limited to times when $U_{10} \leq 7$ m s^{-1} (e.g., Fairall, Bradley, Godfrey, et al., 1996; Webster et al., 1996). Results herein are also consistent with a RL observed in the equatorial western Pacific Ocean during which $U_{10} = 9.5$ m s^{-1} (Wijesekera et al., 1999). In the absence of RLs or DWLs, when the upper ocean was well mixed, U_{10} ranged from 0 to 17.6 m s^{-1} and the 99th percentile value of U_{10} was 13.9 m s^{-1} (Figure 5).

3.3. Occurrence of Stable Layers Throughout the MJO Life Cycle

Of the 44 continuous stable layer events observed, a similar number of events occurred in each of the suppressed, disturbed, and active periods of the MJO (13, 17, and 12 events, respectively) but only 2 stable

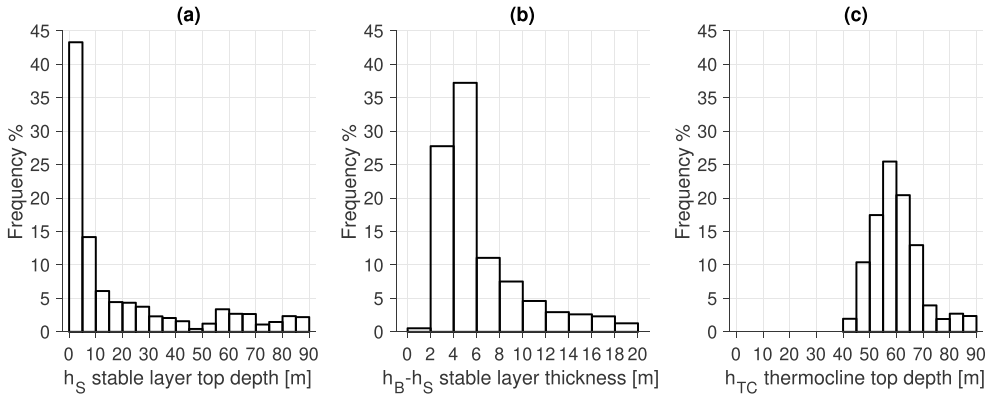

Figure 4. Histograms of observed central Indian Ocean: (a) top depth of stable layers, h_S; (b) thickness of stable layers, $h_B - h_S$; and (c) top depth of thermocline, h_{TC}. Each histogram is normalized by the length of the entire data set.

layer events occurred in the WWB period (Table 2 and Figure 6). The occurrence of RLs and DWLs over the MJO life cycle mirrors the well-documented evolution of U_{10}, R, and Q_{Net} throughout the MJO (Table 1 and Figure 6, e.g., Barnes & Houze, 2013; Johnson et al., 1999; Rickenbach & Rutledge, 1998; Xu & Rutledge, 2015; Zhang, 2005). For example, little rain occurred during the suppressed MJO period (Figure 6 and Table 1). In these conditions, only two RL-DWL events and no RL-only events were observed (Figure 6 and Table 2). During the disturbed and active MJO periods, $U_{10} < 8$ m s^{-1} and rain was frequent, intense, and long lasting (Figure 6 and Table 1; e.g., Xu & Rutledge, 2014). Within these disturbed and active MJO periods, RLs and RL-DWLs occurred once or more per day (Figure 6 and Table 2). During WWBs, when rain was frequent and long lived but U_{10} was very strong, RLs were rarely observed (Figure 6 and Tables 1 and 2). Within WWBs, mean U_{10} = 9.1 m s^{-1} and max U_{10} = 17.6 m s^{-1}, (Figure 6 and Table 1). In contrast, DYNAMO observation days outside of WWBs exhibited much weaker winds, with mean U_{10} = 3.6 m s^{-1} and max U_{10} = 11.3 m s^{-1} (Figure 6 and Table 1).

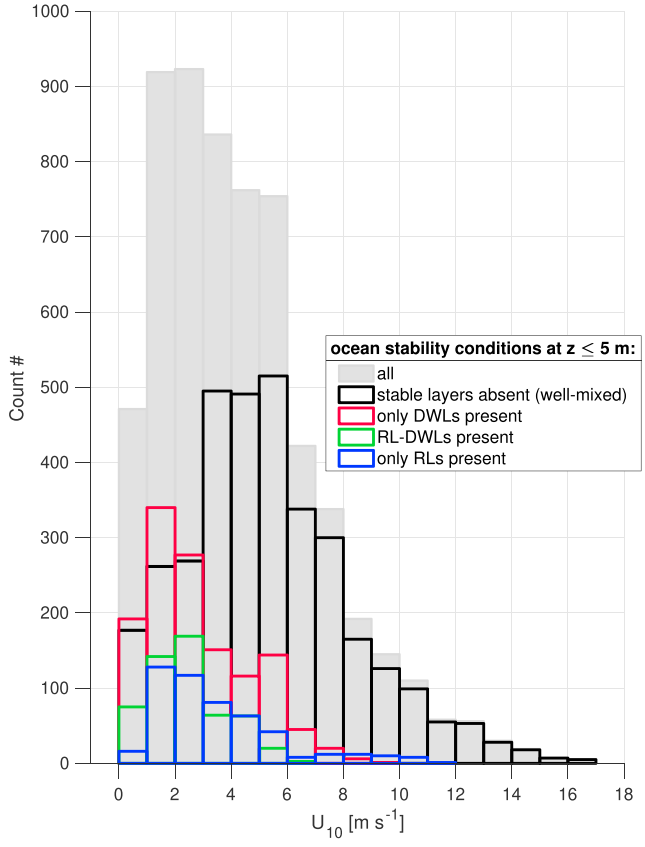

Figure 5. Histogram of U_{10} measured during DYNAMO for different ocean stability conditions at $z \leq 5$ m: All conditions (gray), when no stable layers were present (i.e., when water was well mixed from 0 to 5 m, black), when only DWLs were present (red), when RL-DWL combination layers were present (green), and when only RLs were present (blue). DWL = diurnal warm layer; RL = rain layer; RL-DWL = RL and DWL combination layer.

Similar to the results from previous studies, DWLs consistently formed on days when $Q_{Net} < -600$ W m^{-2} (heating the ocean) and $U_{10} \leq 7$ m s^{-1} (Figures 5 and 6; Asher et al., 2015; Fairall, Bradley, Godfrey, et al., 1996; Matthews et al., 2014; Moulin et al., 2018; Webster et al., 1996). DWLs were not observed when one or both of these conditions were not met, such as on 13 October in the suppressed period, on 19, 24, and 25 October, and on 22 November during disturbed and active periods, and during all WWB days (Figure 6). As a result, DWLs of some form occurred on 92% of observed suppressed period days (all but 1 day), 83% of disturbed MJO days, and 70% of active MJO periods, but DWLs did not occur at all during WWBs (Table 2 and Figures 3 and 6).

Of the 17 DWLs observed outside of the suppressed MJO period, 14 (82%) were actually RL-DWL combinations at one point. In other words, only three DWL-only events were observed during the disturbed and active MJO periods. RL-DWLs combinations occurred in 8 out of 10 observed DWLs during disturbed MJO periods and in 6 out of 7 DWLs during active MJO periods (Figure 6 and Table 2). DWLs and RLs were only observed to overlap once at the beginning of each DYNAMO suppressed phase. No RL-DWL combinations (or DWLS) were observed during WWBs (Figure 6 and Table 2). Overall, RL-DWL combinations only occurred during 9% of the DYNAMO period but totaled to a substantial portion of the total 44 stable layers observed, 16 events or 36%.

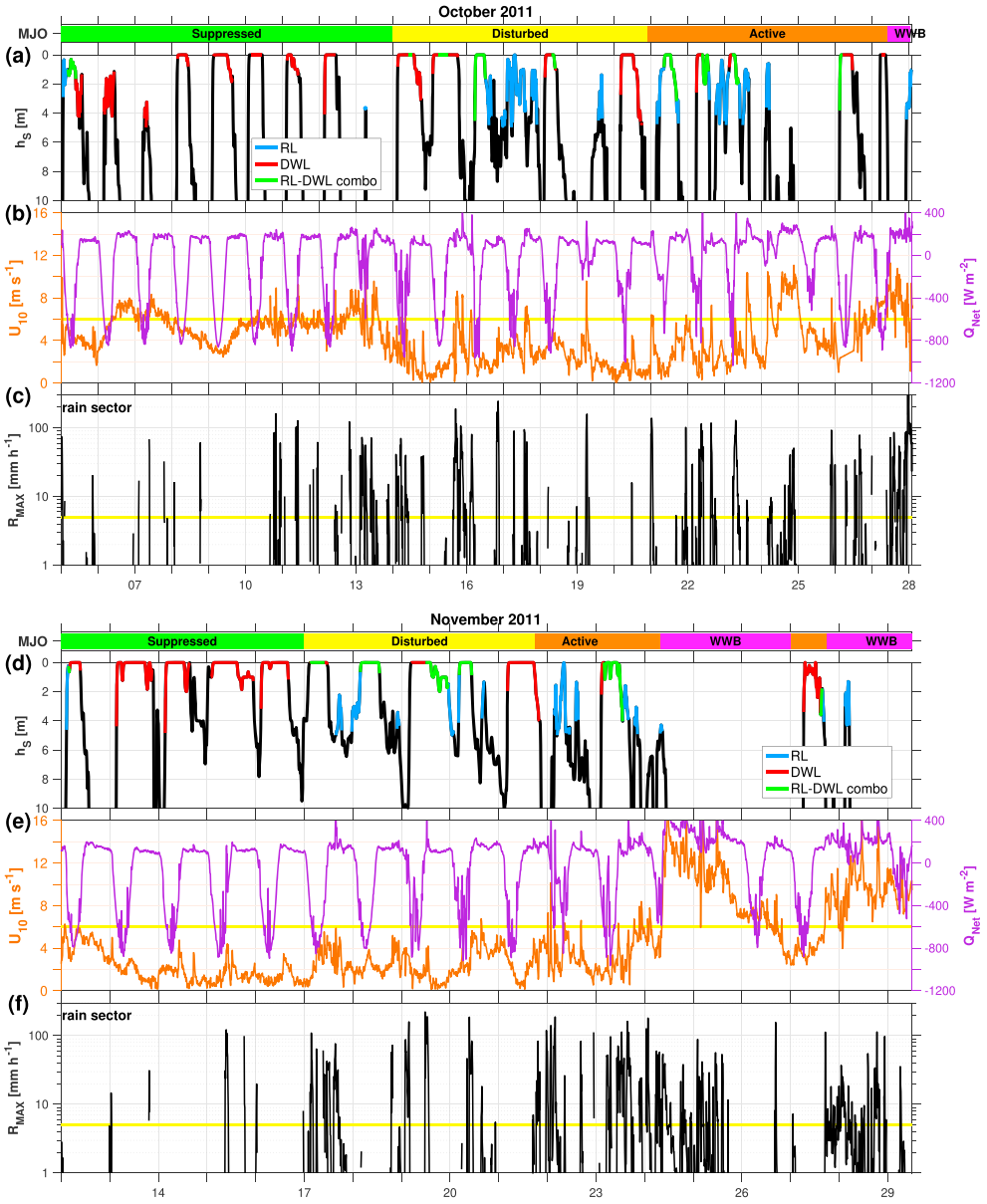

Figure 6. Time series of the observed top depth of ocean stable layers, h_S, colored by stable layer type (a, d); U_{10} and Q_{Net} (b, e); max R observed within the radar rain sector and the ship gauge, R_{MAX} (c, f). Yellow horizontal lines denote $U_{10} = 7$ m s^{-1} and $Q_{Net} = -500$ W m^{-2} in Figures 6b and 6e and $R_{MAX} = 5$ mm h^{-1} in Figures 6c and 6f. The state of the MJO was defined by the RMM index (*WH04*), which corresponds to suppressed, disturbed, active, and westerly wind burst (WWB) time periods in this study (Table 1, section 2.1).

3.4. Diurnal Variability and Duration of Stable Layers

In contrast to DWLs, RLs were observed at all hours of the day and night (Figures 7b and 7e). Out of 32 RLs observed, 18 (56%) existed at some point during overnight hours between sunset (00:30 UTC) and sunrise (12:30 UTC); 20 RLs (62%) existed at some point during the daytime. During DYNAMO, rain occurred at all hours of the day but its intensity peaked in late afternoon and also just before dawn (Figure 7a), as is typically observed over tropical oceans (e.g., Sakaeda et al., 2018; Yang & Slingo, 2001). In alignment with the diurnal cycle of R, RL likelihood also peaked slightly in the afternoon, reaching 29% at 8 UTC (2 p.m. LST, Figure 7b). RL likelihood was at least 7% at all other hours of the day (Figure 7b). Both DWLs and RL-DWLs existed primarily during the daytime (2–22 UTC), with a peak in probability of occurrence between 5 and 10 UTC (11 a.m. to 4 p.m. LST, Figures 7e and 7h). There was a high (66–68%) likelihood of a DWL being

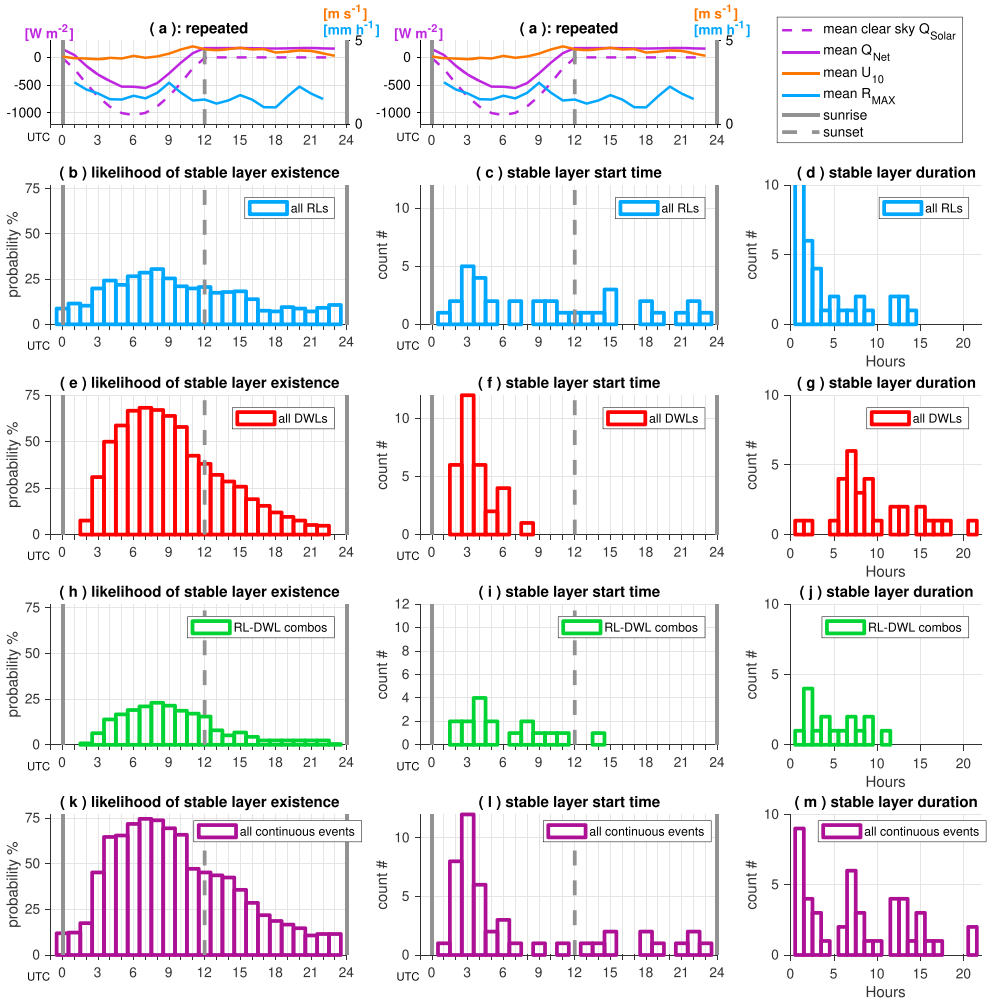

Figure 7. Hourly means of clear-sky Q_{Solar}, Q_{Net}, U_{10}, R_{Max} (a) repeated in both top panels for reference. Hourly likelihood of stable layer existence (b, e, h, k); counts of stable layer start times (c, f, i, l); counts of stable layer durations (d, g, j, m), of *all RLs*, *all DWLs*, *RL-DWL combinations*, and *all continuous stable layer events* regardless of type. The *all RL* and *all DWL* categories (b-d, e-g) include instances of RL-DWLs (h-j), in which RLs and DWLs overlapped. The *all continuous events* category (k-m) considers a time period in which multiple stable layers occurred as one event, so the upper panels do not add to the bottom panel. In this study, sunrise = 00:30 UTC (vertical solid line) and sunset = 12:30 UTC (vertical dashed line), which are marked in the 0th and 12th histogram bins. DWL = diurnal warm layer; RL = rain layer.

present between 6 and 8 UTC (local noon to 3 p.m.). For RL-DWLs, the peak likelihood occurred at a similar time, from 7 to 9 UTC (1–4 p.m. LST), but the peak was not as prominent (19–23%).

Stable layers of all types were less likely to occur at night (Figures 7b, 7e, 7h, 7k). The likelihood of continuous stable layer events, which could contain one or more RLs and/or DWLs, was as low as 10% overnight and as great as 77% at 7 UTC (1 p.m., Figure 7k). At night, the surface cooled ($Q_{Net} > 0$) and hourly-mean U_{10} was slightly greater than in the daytime (Figure 7a). Both of these factors promote convection in the oceanic boundary layer, and could have contributed to the reduced occurrence of stable layers at night.

RLs formed at all hours of the day, but DWLs and RL-DWLs began preferentially during the daytime (Figures 7e, 7f, and 7i). DWLs exhibited a strong peak in hour of formation at 3 UTC, 3 hr after sunrise (Figure 7f). As a result, the peak in formation of all continuous stable layer events was also strongly peaked at 3 UTC (Figure 7l). RLs and RL-DWLs were only slightly more likely to form at 3 and 4 UTC compared to other hours (Figures 7c and 7i).

The average hour in which existing DWLs became absent from the upper 5 m was 14:00 UTC (1.5 hr after sunset). Out of 32 total RLs observed, 11 (34%) formed at night. Four nighttime RLs lasted into the next

daytime cycle, and seven daytime RLs lasted at least 3 hr past sunset. DWLs persisted several hours after sunset during the November suppressed period when a barrier layer existed between 10- to 20-m depth (Figures 3 and 7e). During these very stable upper ocean conditions, DWLs also often formed shortly after dawn.

From the Eulerian perspective of this stationary research ship experiment, RLs were observed locally over durations $\leq$ 14 hr, RL-DWLs were observed for shorter durations ($\leq$ 11 h), and DWLs were observed for the longest durations ($\leq$ 21 hr, Figures 7d, 7j, and 7g). The 21-hr DWL event occurred on 15 November 2011 (Figure 3), having formed at the surface at 2 UTC on top of a salt- and temperature-stratified barrier layer that had risen to within 5–10 m of the surface. By midafternoon, the base of the DWL merged with the underlying barrier layer and the combined near-surface stable layer remained within 5 m of the ocean surface until 23 UTC. Using satellite (Clayson & Bogdanoff, 2013; Stuart-Menteth et al., 2003) and reanalysis (Bellenger & Duvel, 2009) data sets, DWLs have been found to last over 5 days and cover expansive regions of the ocean (1,000 km or more wide). From the Eulerian point of view of the ship, the mean duration of DWLs (10 hr) was double the mean duration of RLs and RL-DWLs (5 hr). The Lagrangian, or water-following, lifetime of stable layers could be longer than suggested by the measurements obtained during DYNAMO. The average duration of all continuous stable layer events was 8 hr (Figure 7m). Minimum RL, DWL, and RL-DWL durations were all 30 min because of the 10-min resolution of this data set. Given the average speed of the surface current during each RL, the equivalent mean and maximum length scales of RLs were 9.2 and 33.2 km. However, this length-scale estimate is approximate because it does not account for lateral mixing of the RL or the spatial and temporal heterogeneity of precipitating systems (Houze et al., 2015; Soloviev & Lukas, 2006; Wijesekera et al., 1999).

The longest-lasting RL was one that formed in a DWL (14 hr). The mean durations of RLs with and without DWL influence were not significantly different. Similarly, DWLs with and without RL influence were not necessarily longer or shorter; both DWL varieties had a mean duration of 10 hr. Ignoring the relative timing of T and S stratification, the overall mean duration of RL-DWL combinations was 5 hr (Figure 7j). RLs that formed on DWLs and DWLs that formed on RLs could be phenomenologically distinct, but a larger data set of these features is required to precisely determine their differences. Thus, these two cases have been combined into a single category, RL-DWLs, for this study.

4. Stable Layer Estimates

This section seeks a better understanding of the observed depth (Figures 3 and 6) and wind limits (Figure 5) of stable layers by examining estimates of each quantity:

1. the top depth of ocean stable layers, $\widehat{h}_S$, and
2. the highest values of U_{10} at which stable layers persist and form, $\widehat{U}_S$.

4.1. Stable Layer Depth: $\widehat{h}_S$

To clarify the relationship between h_S and U_{10}, we consider B, the surface buoyancy flux into the ocean produced by the combined effects of rain and heating (Figure 8, Appendix A, Figure A1, equation A1, Dorrestein, 1979), and u^3_{*W}, the cubed friction velocity in the water, which we consider to represent the rate of TKE input to the ocean surface by the wind; u^3_{*W} (m^3 s^{-3}) is opposed by B (m^2 s^{-3}). The value of B is a function of surface water properties, Q_{Net}, and R. For reference from Appendix A:

1. R = 10 mm h^{-1}, a typical tropical oceanic rain rate (Thompson et al., 2015), produces the same buoyancy as Q_{Net} = −850 W m^{-2}, the median of daytime peak net surface heat fluxes during DYNAMO (Table 1, Figure 6). According to this data set, max R = 188 mm h^{-1} and 30% of R observations exceeded 10 mm h^{-1}, which was also shown by Thompson et al. (2015) for two long-term Indo-Pacific warm pool data sets of R. During DYNAMO, $Q_{Net} < -850$ W m^{-2} during only 1% of observations (min Q_{Net} = −1035 W m^{-2}). Therefore, rain can produce B that is more than an order of magnitude greater than is typically produced by surface heating (Figure 8).
2. The buoyancy produced by R = 5 mm h^{-1} is equal and opposite to the buoyancy destroyed by a surface cooling on the order of Q_{Net} = 400 W m^{-2}, which is the maximum nighttime Q_{Net} outside of WWB periods and maximum observed latent heat flux, Q_{Lat}. Since R = 5 mm h^{-1} is a relatively weak rain rate and Q_{Net} = 400 W m^{-2} is a very high cooling rate, buoyancy produced by rain typically stabilizes negative buoyancy produced by surface cooling.

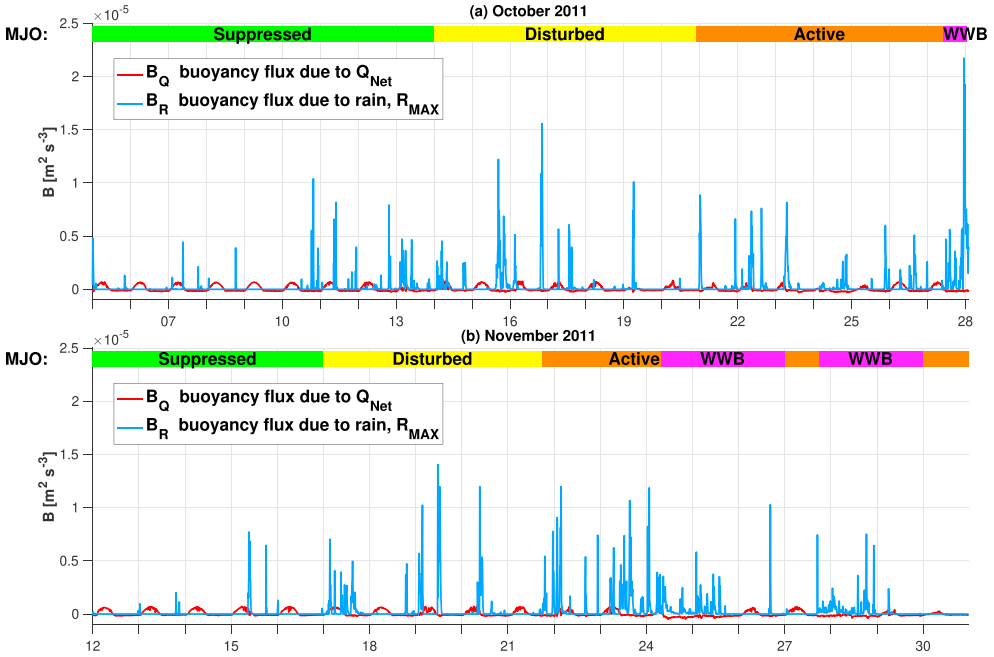

Figure 8. DYNAMO measured buoyancy flux, B, due to heating, cooling, and evaporation by Q_{Net}, B_Q, and due to the net effect of rain freshening and rain cooling by R_{MAX}, B_R (Appendix A). The state of the MJO was defined by the RMM index (*WH04*), which corresponds to suppressed, disturbed, active, and westerly wind burst (WWB) time periods in this study (Table 1, section 2.1).

3. Buoyancy produced by rain freshening is 15 times greater than negative buoyancy produced by rain cooling (Figure 8), meaning the cooling effect of rain on B can be ignored. B produced by rain is always positive, which can lead to stratification of the upper ocean.

From a 1-D perspective and neglecting shear- and wave-driven turbulence, Monin-Obuhkov scaling suggests that B will be mixed by wind stress to an estimated depth of $\widehat{h}_S$ given by

$$\widehat{h}_S = \frac{u_{*W}^3}{\kappa B} \tag{7}$$

where $\kappa = 0.40$, the von Kármán constant, or

$$\widehat{h}_S = C\frac{U_{10}^3}{B} \tag{8}$$

where the constant C includes the densities of seawater and air, ρ_W and ρ_{air}, and a drag coefficient, $C_D \sim 0.8–1 \times 10^{-3}$ (Edson et al., 2013):

$$C = \frac{1}{\kappa}\left(\frac{C_D\rho_{air}}{\rho_W}\right)^{3/2} \cong 5.42\times10^{-9} \tag{9}$$

Equations (8) and (9) arise from the fact that the flux of momentum is continuous across the sea surface such that $\tau = \rho_W u_{*W}^2 = \rho_{air} u_{*air}^2$, where the τ in the air is approximated by $C_D\rho_{air}U_{10}^2$.

According to observations, if surface water is less dense than underlying water, $h_S \sim 0$ m and h_S marks the top of a stable layer that is in contact with the surface (Figures 2 and 3). In (7) and (8), $\widehat{h}_S \sim 0$ for very large B and weak values of u_{*W}^3 or U_{10}, respectively. Equations (7) and (8) result from the assumption that the stable layer depth, h_S, responds to changing production and consumption of TKE. This approach is in contrast to a Richardson number constraint, which is applied with mixed layer models or simple layer-averaged slab models (Fairall, Bradley, Godfrey, et al., 1996).

By isolating DYNAMO data for periods when $B > 0$, close agreement was found between $\widehat{h}_S$ and h_S (Figure 9, in which h_S was temporally averaged by a 1-hr moving mean filter and $\widehat{h}_S$ was temporally averaged by a 2-hr

moving mean filter). Of 44 total observed stable layers, 36 were successfully predicted to exist at $z \leq 5$ m by $\widehat{h_S}$within the same time span that they occurred according to h_S (Figure 9). This equates to an 88% success rate in terms of stable layer prediction. All DWLs, all RL-DWLs, and all but eight short-lived RLs were predicted by $\widehat{h_S}$. During times when $\widehat{h_S}$ mirrored h_S, we assume that the buoyancy and wind mixing forces described in (7) and (8) were the dominant factors controlling the depth of upper ocean stratification, h_S. When $B < 0$, the ocean should mix vertically due to convective overturning by surface cooling or extreme salinification. However, when $B < 0$, $\widehat{h_S}$ also becomes negative, the latter of which is nonphysical and is therefore not shown in Figure 9**.** The estimated stable layer depth $\widehat{h_S}$ was able to account for observed near-surface stratification better than the observed mean value, $\overline{h_S}$ = 20 m, or the monthly mean mixed layer depths, h_{M1} and h_{M2}, determined by two previous studies for this location in October and November (Figure 9**,** de Boyer Montégut et al., 2004: 17 and 19 m; Holte et al., 2017: 34 and 37 m, respectively). The oscillation of h_S between its two extrema, near-surface stratification or deep mixing, was not random. In other words, h_S did not randomly vary about $\overline{h_S}$. Rather, the h_S oscillations systematically coincided with the occurrence of either buoyancy production by rain and solar heating, or buoyancy destruction by wind (Figures 6, 8, and 9).

Several 1- to 2 hr temporal differences existed between estimated $\widehat{h_S}$ and observed h_S (Figure 9). These temporal differences appear reasonable given that h_S is an observation of a present state, whereas $\widehat{h_S}$ is a prediction of a future equilibrated state given the present values of B and U_{10}. Moreover, temporal and spatial averaging were performed in the estimation of both $\widehat{h_S}$ and h_S time series, and S measurements were not collected at $z < 2$–3 m. For instance, the 1- to 2-hr temporal differences between $\widehat{h_S}$ and h_S appear understandable because RLs initially form within the top several centimeters of the ocean (Drushka et al., 2016), they often propagate laterally (Soloviev et al., 2015), and a finite amount of time is required for freshwater to be mixed and diffused downward past the 2- to 3-m salinity measurements used in this study (Asher et al., 2014). All of these aforementioned issues and processes could have contributed to the frequently observed 1- to 2-hr timing offset between h_S and $\widehat{h_S}$.

Aside from these slight timing differences, three additional differences were evident between $\widehat{h_S}$ and h_S (Figure 9):

1. *False Negatives*. Eight RLs were observed but not predicted, all of which occurred after sunset on 17, 19, 22, 27 October and 18, 19, 20, 22 November (e.g., second RL in Figure 2 for 22 October). These RLs were 1.5–4 hr in duration. Local rain occurred during only two of the missed RLs, whereas upstream rain was observed within 3 hr of all eight events. These RLs may have resulted from advection of near-surface freshwater. This could have led to their underprediction by $\widehat{h_S}$, which relies on current conditions to predict stable layer existence. One of the missed RLs formed inside a DWL that was correctly predicted and that was already in contact with the barrier layer (on 19 November).
2. *False Positives*. Three RLs were predicted but not observed. These occurred during WWBs when contemporaneous *Revelle* measurements showed that subsurface turbulence was higher than would be expected from wind alone, having been enhanced by shear across a 50- to 100-m depth Wyrtki Jet (Moum et al., 2014).
3. *Underpredicted Duration*. Several DWLs, RLs, and RL-DWLs were observed to last longer than predicted. DWLs and RLs can harbor stability near the surface well after B ceases to be positive, particularly if U_{10} is weak, according to model simulations by Drushka et al. (2016). For instance, several DWLs lasted 3 hr after sunset and the maximum observed duration of DWLs and RLs was 21 and 14 hr, respectively (Figure 7). Therefore, the duration of some stable layers exceeded the length of daytime (12 hr in this study) and also the duration of any individual rain event. Some of the stable layers with underestimated duration occurred when the surface stable layers merged with the underlying barrier layer (Figure 4), meaning that the barrier layer could have influenced the life cycle of certain stable layers. Underpredicted stable layer duration could also result from underestimates of surface freshwater advection. The value of B was calculated with R_{MAX}, the maximum R observed from either the ship's gauges or the ship's radar within a sector spanning 9 km in the upstream direction (roughly a 3-hr advective time scale) and 4 km in all other directions (section 2**,** Figure 1). We acknowledge the limitation of this method to account for the spatial heterogeneity of B due to rain.

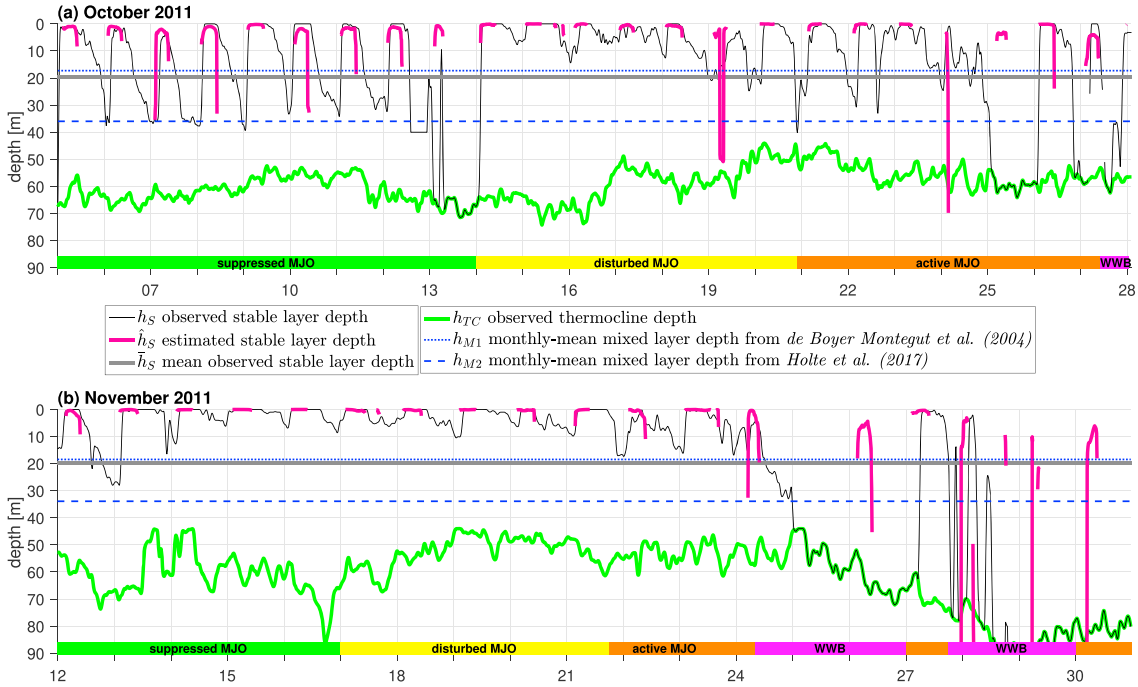

Figure 9. DYNAMO observed stable layer top depth (h_S), estimated stable layer top depth from surface fluxes $\left(\hat{h}_S\right)$, mean observed stable layer top depth ($\overline{h_S}$), observed thermocline top depth (h_{TC}), and monthly-mean mixed layer depths (h_{M1} and h_{M1}) for this location in October and November 2011 according to climatologies by de Boyer Montegut et al. (2004, h_{M1}) and Holte et al. (2017, h_{M2}). The state of the MJO was defined by the RMM index (*WH04*), which corresponds to suppressed, disturbed, active, and westerly wind burst (WWB) time periods in this study (Table 1, section 2.1).

4.2. Stable Layer Wind Limit: $\widehat{U}_S$

Equations (8) and (9) can be rearranged to describe the wind limit of stable layers, $\widehat{U}_S$, defined as the highest value of U_{10} in which stratification should exist at the depth h_S for a given value of B:

$$\widehat{U}_S = \left(\frac{\hat{h}_S B}{C}\right)^{1/3} \cong 569\left(\hat{h}_S B\right)^{1/3} \tag{10}$$

If $B > 0$ and $U_{10} \leq \widehat{U}_S$, then conditions should be favorable for the formation and persistence of stable layers at depths of $z \leq h_S$. On the other hand, if $B > 0$ but $U_{10} > \widehat{U}_S$, surface-forced mixing should outweigh buoyancy suppression and neither DWLs nor RLs should form at $z \leq h_S$. In other words, wind mixing will homogenize T and S in a layer extending from the surface downward to the barrier layer or the thermocline (Figures 3 and 9).

Solutions for (7), (8), and (10) appear in Figure 10 for h_S = 1, 2, and 5 m: ${u_{W*}}^3$ and B are related linearly (Figure 10a), whereas $\widehat{U}_S$ is proportional to $B^{1/3}$ (Figure 10b). In these figures, lines of constant h_S show that stable layers should form at these depths for a given B and u^3_{*W} (Figure 10a) and therefore U_{10} (Figure 10b, equations (7), (8)). Alternatively, the lines of constant h_S also indicate the highest values of U_{10} that can take place while stable layers either form or persist for a given B. From (10), the stable layer wind limit, $\widehat{U}_S$, is equal to 8.6 m s^{-1} for R = 50 mm h^{-1} and h_S = 1 m, which means that R = 50 mm h^{-1} should maintain a RL with stable dS/dz gradients as shallow as 1-m depth so long as $U_{10} \leq$ 8.6 m s^{-1}. For the same R value and h_S = 5 m, the wind limit of RLs increases to $\widehat{U}_S$ = 13.6 m s^{-1}, which is only slightly higher than the greatest value of U_{10} observed in a RL: 11.3 m s^{-1} (Figure 5). Values of $\widehat{U}_S$ range between 8.0 and 13.6 m s^{-1} for R between 10 and 50 mm h^{-1}, while $\widehat{U}_S$ = 8.4 m s^{-1} for the strongest surface heating observed: $Q_{Net} = -1035$ W m^{-2} (10). This estimated wind limit on DWLs is close to the observed wind limit, U_{10} = 7.6 m s^{-1} (the 99th percentile value of U_{10} when DWLs were present, Figure 5). An additional interpretation of these calculations is that a DWL may

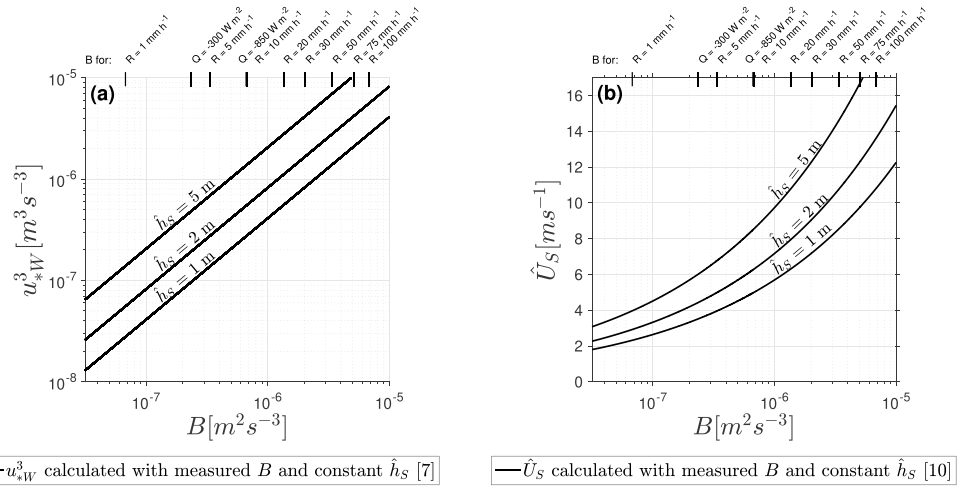

Figure 10. Calculated (a) u^3_W and (b) $\widehat{U}_S$ using different stable layer depths of h_S = 1, 2, and 5 m and measured B in (7) and (10). The value of $\widehat{U}_S$ is the highest value of U_{10} at which wind mixing and B should support the existence of a stable layer at depth h_S. Examples of B for various net heat fluxes (Q_{Net} abbreviated as Q in plot) and rain rates (R) are shown atop each plot for reference.

persist at z ≤ 5 m when U_{10} = 8.4 m s^{-1} if Q_{Net} is maximized (−1035 W m^{-2}), while a RL may persist at the same depth and during the same wind speed even if R is only moderate (12 mm h^{-1}). Since instances of $R > 12$ mm h^{-1} are frequent, (8) and (10) can explain observations of RLs persisting at higher U_{10} than DWLs (Figures 5 and 10).

For all instances in which stable layers were present, 46% of DWL only, 70% of RL only, 70% of RL-DWL, and 66% of all stable layer instances occurred when $U_{10} < \widehat{U}_S$ and $B > 0$ m^2 s^{-3}, and when $\widehat{U}_S$ was evaluated with (10) assuming h_S = 5 m. These percentages represent the success rates at which near-surface stable layer occurrence can be estimated by determining times when $U_{10} < \widehat{U}_S$ and $B > 0$ m^2 s^{-3}.

The $\widehat{h}_S$ and $\widehat{U}_S$ methods predicted 36 out of 44 total stable layers to occur within the same time span that they were observed, leading to an overall success rate of 88% (Figure 9). The remaining eight missed stable layers were RLs of relatively short duration, between 1.5 and 4 hr, that occurred within 6 hr of other observed (and successfully predicted) stable layers (Figure 9). In other words, all observed DWLs, all observed RL-DWLs, and 75% of observed RLs were successfully predicted to occur within observed stable layer time spans.

The occurrence of $U_{10} < \widehat{U}_S$ and $B > 0$ m^2 s^{-3} was much more likely prior to the WWB (Figures 5, 8, and 9). Values of U_{10} were rarely low enough to support stable layers during WWBs, despite high B during this period (Figures 8 and 9). For example, only three RLs and no DWLs were observed in WWBs. In suppressed, disturbed, and active MJO periods, conditions in which $U_{10} < \widehat{U}_S$ and $B > 0$ m^2 s^{-3} occurred at least once per day (Figures 5 and 9). Stable layers were frequently observed and predicted to occur during these periods (Figure 9).

Both U_{10} and R were necessary for determining the likelihood of RL formation (Figure 11), while Q_{Net} alone could serve as a useful predictor for DWL occurrence (Figures 5 and 11). For example, DWLs were only present during 15% of the time when $Q_{Net} > 0$ W m^{-2}, and never formed in these conditions, whereas DWLs were present 99% of the time when $Q_{Net} < -600$ W m^{-2} (Figure 11a). The value of $Q_{Net} < -500$ W m^{-2} during every observed DWL (Figures 11a and 6). Thus, to a certain extent, the magnitude of Q_{Net} was a useful predictor of DWL occurrence even without consideration of U_{10} (Figure 11b). In contrast, many instances of R = 0 mm h^{-1} occurred leading up to RL formation and when a RL was present. The probability distribution functions of R were also not statistically different between times with or without the presence of a RL (Figure 11b). In other words, RLs were not statistically more likely to occur at any R range except when $R > 100$ mm h^{-1}, and these high rain rates represent a small fraction of the total R distribution. Therefore, the $\widehat{h}_S$- and $\widehat{U}_S$-based estimate of stable layer occurrence, which incorporates both U_{10} and B (i.e., R), was more successful in determining the likelihood of RL formation compared to predicting the existence of a RL using R alone (Figure 11d).

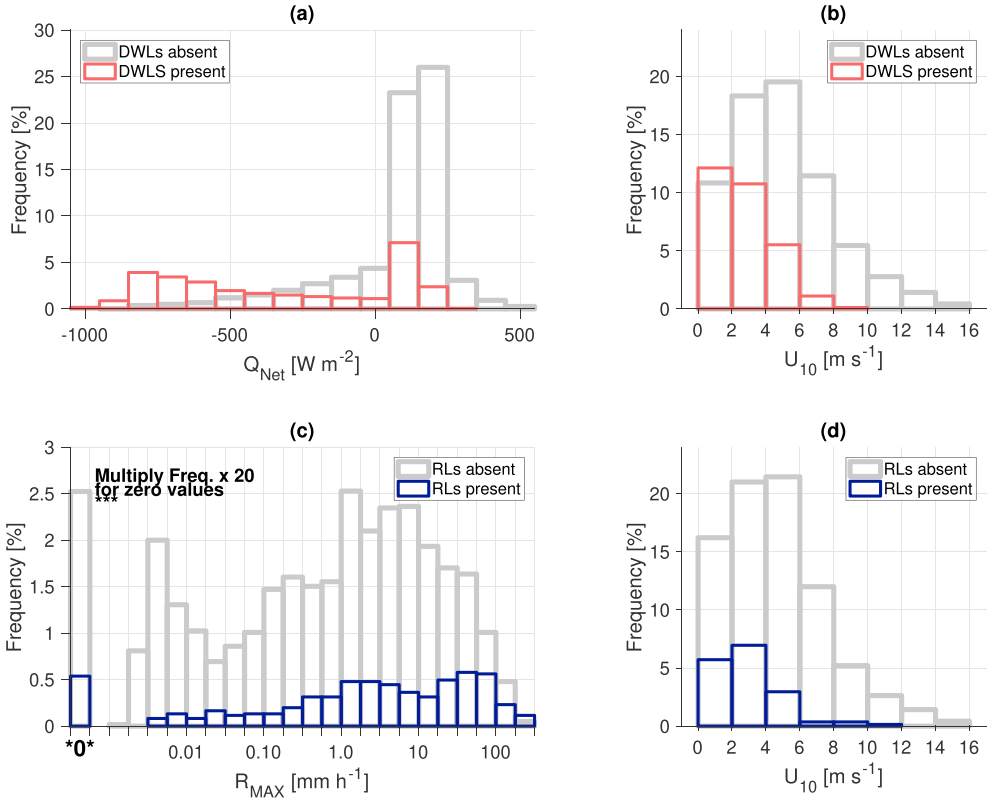

Figure 11. Histograms of Q_{Net}, U_{10}, and R_{MAX} (max R observed within rain sector of Figure 1) in either the absence or presence of DWLs (a, b) or RLs (c, d) normalized by length of data set. DWLs = diurnal warm layers; RLs = rain layers.

5. Discussion

The presence of near-surface stable layers is important for coupled climate processes because they limit the vertical extent of wind-driven ocean mixing and the distribution of atmospheric forcing into the ocean (e.g., Fairall, Bradley, Godfrey, et al., 1996; Price et al., 1986). When DWLs, RLs, or their combinations are present, turbulence must first supply enough kinetic energy to homogenize the near-surface stable layers before mixing can extend deeper into the ocean column. While formation of a DWL is limited to daytime since it requires solar warming, a RL can form at any time. Furthermore, a RL may form within an existing DWL, and a DWL may form within an existing RL (Figures 2 and 6). These two cases are considered together as RL-DWL combinations in this study, though they could be phenomenologically distinct.

Based on the stable layer observations and estimates presented in sections 3 and 4**,** we hypothesize that the top depth of RLs and DWLs, h_S, can be reasonably predicted as $\widehat{h}_S$ in terms of U_{10} and B and that the upper limit of U_{10} at which RLs and DWLs can form and persist, U_S, can be estimated in terms of B. This suggests that reasonable estimates of $\widehat{h}_S$ might be produced from data sets of U_{10} and B over tropical oceans in which neither advection nor current shear are dominant forces in the budgets of ocean buoyancy or momentum (Figure 9). Measurements of U_{10} and B are collected by moorings, ships, autonomous vehicles, and satellites. Estimates of U_{10} and B are also available from several global products based on observations, such as reanalysis, TropFlux (Praveen Kumar et al., 2012), and SeaFlux (Curry et al., 2004). Therefore, without the use of subsurface ocean measurements, the $\widehat{h}_S$ and $\widehat{U}_S$ estimates could help determine when and where the vertical extent of ocean mixing is limited to shallow depths of $z \leq 5$ m.

Furthermore, we hypothesize that the occurrence of RLs and DWLs throughout the MJO is regulated by intraseasonal variations in U_{10}, Q_{Net}, and R, as well as the local balance between B and U_{10} (Table 2 and Figures 6 and 9). Throughout the two MJO cycles observed during DYNAMO, RLs withstood $U_{10} \leq 9.8$ m s^{-1}, while DWLs only survived $U_{10} \leq 7.6$ m s^{-1} (99th percentile values). RLs were also much less likely to occur when

R_{MAX} decreased below 5 mm h^{-1} (Figure 8), which can explain the rare occurrence of RLs during suppressed MJO periods when $U_{10} < 8$ m s^{-1} but when sky conditions were mostly clear with little rain (Figure 6). RLs and RL-DWLs were most likely to occur during disturbed and active MJO periods, which exhibit frequent, heavy rain, and $U_{10} <$ 8–9 m s^{-1} (Table 1) During WWBs, $U_{10} >= 7$ m s^{-1}, leading to only two observed RLs despite persistently high B from rainfall during this period (Figures 6, 8, and 9). WWB conditions, characterized by both net surface cooling and high U_{10}, were even less suitable for DWL formation: no DWLs were observed during WWB periods. Near-surface stratification during WWB periods was also diminished by shear-driven turbulence generated from a Wyrtki Jet in the upper 50–100 m (Moum et al., 2014). DWLs without RL influence were most common in suppressed periods when strong net ocean heating occurred in conjunction with little rain and light wind conditions ($U_{10} < 7$ m s^{-1} during 95% of suppressed periods, Figure 6). DWLs also occurred in disturbed and active periods, but 83% of these occurred in combination with RLs at some point (Table 2 and Figures 6 and 9).

The different phasing of DWL occurrence versus RL occurrence relative to MJO evolution could have implications for tropical air-sea interaction (DeMott et al., 2014, 2015, 2016; Zhang, 2005). The influence of DWLs on ocean mixed layer temperature, SST, air-sea fluxes, and precipitation in suppressed MJO periods has already been well established in previous studies (Bellenger et al., 2010; Chen et al., 2015; Johnson & Ciesielski 2017; Matthews et al., 2014; Ruppert 2016; Ruppert & Johnson, 2015; 2016; Seo et al., 2014; Shinoda & Hendon, 1998). In disturbed and active MJO periods, RLs and RL-DWLs each formed at least 4 times more often than DWLs alone (Table 2 and Figure 6). The most intense atmospheric convection tends to occur at the beginning of the active MJO period, according to radar data shown by Xu and Rutledge (2014). During WWBs, U_{10} is strongest (sustained values $>$ 7 m s^{1}; Figure 6), net surface cooling is more common ($Q_{Net} > 0$; Table 1 and Figure 6), and a greater percentage of rain accumulation is stratiform (longer duration and lighter intensity, quantified by Xu & Rutledge, 2014).

Rain's impact on near-surface ocean stability and mixing throughout the MJO should not be ignored. Throughout the two MJOs, RLs created conditions during which turbulence was limited to the upper few meters of the ocean rather than the seasonal mean mixed layer depth described by climatologies from Argo floats and ship CTD profiles (conductivity temperature depth) (Figure 9). RLs were observed to form at least as often as DWLs (32 versus 30 events), several RLs were observed to persist locally for 10–14 hr, and RLs were observed at all times of the day and night (Table 2 and Figures 6 and 7). Since RLs played a significant role in establishing near-surface ocean stratification (occupying 16% of the data set), analysis of upper ocean stability based on temperature or DWLs alone is incomplete outside of suppressed MJO periods.

Global investigations of RL coverage have not yet been completed. Similar to this study's findings, RLs at other latitudes are also likely to cover smaller areas and shorter time period than DWLs due to the localized area and short duration of rain events compared to the coverage of cloud-free, low-wind conditions required to form DWLs. Large areas of tropical, subtropical, and midlatitude oceans may be cloud free at any given time. In contrast, rainfall is narrowly concentrated across equatorial latitude bands due to the Intertropical Convergence Zone, monsoons, and the MJO, as well as broadly distributed across the midlatitudes associated with the passage of large low-pressure systems (e.g., Pendergrass & Deser, 2017). If the sensitivity of RL formation and persistence to U_{10} is also considered, the global coverage and frequency of RLs would be even lower than suggested by rain climatologies alone. This hypothesis was confirmed by simulations conducted by Drushka et al. (2016) for tropical regions using a 1-D turbulence-allowing ocean model and reanalysis data.

Results presented herein should motivate future studies regarding coupled numerical models and observational analysis. The tendency for DWLs and RLs to coexist (16 continuous events) and for overnight RLs to last into the next daytime cycle (4 events) suggests that parameterizations for near-surface stratification should be designed so that RLs and DWLs can form in the same place and evolve concurrently. The results indicate that RL formation and persistence were strongly related to instantaneous rain rate, R, on 10-min time scales. Therefore, the accuracy of predicted or assimilated rain on these time scales will impact the fidelity of simulated upper ocean stratification in numerical models. Model mixing schemes will also determine the simulated impacts of rain and surface warming on the ocean. Since RLs, DWLs, and their combinations were typically between 2- and 4-m thick vertically with $h_S \leq 5$ m (Figure 4), 1-m vertical resolution in the upper

5–10 m appears critical for observational and modeling experiments regarding RLs and DWLs. Argo floats, bathythermograph measurements, and most moorings have historically observed S and T at 1- to 5-m depth with 2-m vertical resolution, which have not consistently captured near-surface RLs or DWLs (Anderson & Riser, 2014; Gould & Turton, 2006). The frequent occurrence of RLs and DWLs in tropical oceans would also be completely ignored in coupled model results that rely on mean or slab mixed layer depths. A review of MJO air-sea coupled processes by DeMott et al. (2015) does not recommend configuring coupled models with mean or slab-ocean mixed layer depths. For instance, the DYNAMO stable layer depth, h_S, was only within ±5 m of the 20-m mean value of h_S for 9% of this data set. The dominant modes of variability in the upper Indian Ocean observed throughout two MJOs during DYNAMO can be more accurately summarized in two ways (Figure 9): (1) rain and/or diurnal heating stabilized the upper 5 m of the ocean and limited mixing to these shallow depths on 37 out of 42 days, 38% of the time; (2) turbulence and ocean convection mixed the water from the surface to at least 40-m depth on 20 out of 42 days, 62% of the time.

6. Conclusions

Near-surface ocean stable layers limit the penetration depth of wind mixing and the vertical distribution of atmospheric fluxes of momentum, freshwater, and heat. Therefore, the presence of near-surface ocean stable layers can amplify variability in both SST and SSS. Leading up to this study, diurnal warm layers (DWLs) resulting from surface heating were more comprehensively understood compared to RLs resulting from precipitation; both rain layers (RLs) and DWLs are statically stable near-surface layers. While DWLs were known to frequent the low-wind, high-insolation suppressed period of the MJO, the frequency at which RLs or their combinations with DWLs occurred throughout the MJO was unknown. The current study used central Indian Ocean ship-based observations of rain, wind, and vertical gradients of ocean temperature and salinity to better understand the following features of RLs, DWLs, and RL-DWLs: their formation and persistence as a function of U_{10} and B, as well as their occurrence as a function of MJO phase. Tracking of 30 DWLs, 32 RLs, and 17 RL-DWL combinations from a stationary research vessel revealed, throughout two MJO events, the following:

- RLs and DWLs stabilized the ocean at depths of $z \leq 5$ m in 38% of the data set.
- Although RLs were more numerous than DWLs, 32 versus 30 events, RL duration was usually shorter. RLs and RL-DWLs were observed with durations ≤ 14 and ≤ 11 hr (mean duration = 5 hr), whereas DWLs were observed with longer durations ≤ 21 hr (mean duration = 10 hr).
- During 16% of the data set, RLs of some kind occurred; in 30% of the data set, some form of DWLs occurred.
- RLs and RL-DWL combinations primarily formed in disturbed and active MJO conditions, usually forming at least once per 24 hr in these periods.
- DWLs without RL influence usually occurred daily in suppressed MJO conditions and occurred rarely thereafter.
- Of the 17 DWLs that occurred in the disturbed and active MJO periods, all but three combined with an RL at some point.
- During WWB conditions, DWLs were not detected and RLs formed rarely.
- When DWLs were present, 99% of U_{10} values were below 7.6 m s^{-1}. When RLs were present, 99% of U_{10} values were below 9.8 m s^{-1}.
- RLs contained enough buoyancy to withstand nocturnal ocean convection and surface cooling. RLs forming during the day were often observed to persist through the day-to-night transition. RLs forming at night were often observed to persist through the night-to-day transition.
- An estimate for stable layer depth, $\widehat{h}_S$, was developed based on U_{10} and the buoyancy flux, B. This led to an estimate for $\widehat{U}_S$, the maximum U_{10} at which stable layers should exist at depth h_S for fixed B. These stable layer estimation methods predicted 88% of the observed stable layer events (36 out of 44 events) during the time span in which they were observed.
- The different occurrence rate of RLs versus DWLs throughout the MJO cycle appears to be explained by variations in Q_{Net}, R, and U_{10} throughout the MJO, and by the fact that RLs can withstand higher U_{10} than DWLs. For instance, RLs and RL-DWL combinations tended to occur in disturbed and active MJO periods, whereas DWLs alone were more frequent in suppressed MJO periods.
- The 20-m mean value of stable layer depth, $\overline{h_S}$, was almost never observed. Use of $\overline{h_S}$ in place of observed h_S would have led to an overestimation or underestimation of the penetration depth of wind mixing in

91% of the data set, in which case errors exceeded 100%. Similar errors would have been caused by monthly mean mixed layer depths derived from climatologies of Argo profiles, which were similar to this study's estimate of $\overline{h_S}$.

- The distribution of observed stable layer depth, h_S, was bimodal, centered at 0–5 m during near-surface stable layers or centered at 40–70 m when water was well mixed from the surface to the thermocline.

Appendix A: Surface Buoyancy Flux Into the Ocean

From Dorrestein (1979), the surface buoyancy flux into the ocean is

$$B = \frac{g}{\rho_W}\left[S_0\beta(P-E) - \frac{\alpha}{c_p}(Q_{\mathrm{Lat}} + Q_{\mathrm{Sens}} + Q_{\mathrm{Solar}} + Q_{\mathrm{IR}}) + \alpha\Delta TP\right] \quad \text{(A1)}$$

Rain Freshening and Evaporation Term | Heating Term | Rain Cooling Term

Table A1 explains the variables, constants, and typical values for components of B in (A1). The first term of (A1) conveys how the precipitation mass flux, P, makes the surface layer more buoyant (less dense), whereas evaporation mass flux, E, increases surface salt content and therefore increases surface seawater density. The second term of (A1) describes the generation of buoyancy by surface heating (stabilization) and the destruction of buoyancy by surface cooling (destabilization). Similar to the heating term of (A1), the rain cooling term of (A1) accounts for surface heat loss and layer destabilization by the rain-sea temperature difference (Fairall, Bradley, Rogers, et al., 1996; Gosnell et al., 1995).

To evaluate (A1), the rain rate, R, must be multiplied by the density of pure water, ρ_{PW} = 1,000 kg m^{-3}, to determine the precipitation mass flux, P, in kg m^{-2} s^{-1}:

$$P = \rho_{\mathrm{PW}}R \quad \text{(A2)}$$

Similarly, the evaporation mass flux, E, in kg m^{-1} s^{-1}, is determined by

$$E = Q_{\mathrm{Lat}}L_V^{-1} \quad \text{(A3)}$$

where L_V is the latent heat of vaporization, 2.25×10^6 J kg^{-1} to 2.5×10^6 J kg^{-1} at 100 °C to 0 °C, respectively.

When evaluated with central Indian Ocean observations of fluxes, R, and surface water properties, B is widely distributed between -3×10^{-7} and 2×10^{-5} m^2 s^{-3} (Figure A1). The most frequent values of B are negative, corresponding to persistent evaporation and cooling by the sensible, latent, and radiative heat fluxes (minimum Q_{Net} = 400 W m^{-2}). The maximum rate of evaporation that was observed during DYNAMO was 0.6 mm h^{-1}, over 2 orders of magnitude lower than the maximum rain rate that was observed: 184 mm h^{-1} measured within 8 km upstream of the ship radar and 96 mm h^{-1} measured by the ship rain gauge. Compared to the net heat flux, rain produced values of B that were distributed over a wider range and were of much greater magnitude (Figure A1). Equation (A1) shows that equivalent B is produced by the median value of daytime peak heating rates, Q_{Net} = −850 W m^{-2}, and a relatively weak rain rate of R = 10 mm h^{-1}. Peak daytime Q_{Net} observed during DYNAMO was −1,035 W m^{-2}, which produced only slightly larger B (Figure A1).

B due to interfacial turbulent and radiative heat exchanges, B_{Q}, can be systematically separated from B contributed by rain, B_{R}:

$$B = B_{\mathrm{Q}} + B_{\mathrm{R}} \quad \text{(A4)}$$

$$B_{\mathrm{R}} = \frac{g}{\rho_W}P(S_0\beta + \alpha\Delta T) \quad \text{(A5)}$$

$$B_{\mathrm{Q}} = \frac{g\alpha}{\rho_W c_P}\left[\left(1 - \frac{\beta c_P}{\alpha L_V}S_0\right)Q_{\mathrm{Lat}} + Q_{\mathrm{Sens}} + Q_{\mathrm{Solar}} + Q_{\mathrm{IR}}\right] \quad \text{(A6)}$$

Table A1
Components of the Surface Buoyancy Flux Into the Ocean

Name	Term	Value
Gravitational constant	g	9.81 m s^{-2}
Seawater density	ρ_W	1,022 kg m^{-3}
Sea surface salinity	SSS	33.7 to 35.5 PSU
Sea surface temperature	SST	28.5 to 32.0 °C
Precipitation mass flux	P	0 to 0.0936 kg m^{-2} s^{-1}
Evaporation mass flux	E	9×10^{-6} to 2×10^{-4} kg m^{-2} s^{-1}
Thermal expansion coefficient	α	3.2×10^{-4} to 3.5×10^{-4} °C^{-1}
Salt contraction coefficient	β	7.32×10^{-4} to 7.35×10^{-4} PSU^{-1}
Specific heat of seawater	c_P	3997 to 4007 J K^{-1} kg^{-1}
Latent heat flux	Q_{Lat}	22 to 410 W m^{-2}
Sensible heat flux	Q_{Sens}	−0.5 to 100 W m^{-2}
Net solar heat flux	Q_{Solar}	−1200 to 0 W m^{-2}
Net infrared heat flux	Q_{IR}	18 to 77 W m^{-2}
Rain-sea temperature difference	$\Delta T = T_W - SST$	−2.3 to −6.9 °C
Wet bulb temperature	T_W	23.3 to 26.3 °C
Rain freshening and evaporation term	$S_0\beta(P - E)$	-2.6×10^{-6} to 2.4×10^{-3} kg m^{-2} s^{-1}
Heating term	$-(\alpha/c_P)\ Q_{Net}$	-4.4×10^{-5} to 8.7×10^{-5} kg m^{-2} s^{-1}
Rain cooling term	$\alpha P \Delta T$	-1.3×10^{-4} to 0 kg m^{-2} s^{-1}
First term	g/ρ_W	9.6×10^{-3} kg^{-1} m^4 s^{-2}
Total buoyancy flux	B	-1.2×10^{-7} to 8.8×10^{-6} m^2 s^{-3}

Note. Variables, constants, and values for components of the ocean surface buoyancy flux B (A1) are evaluated with DYNAMO data from the current study. Heat fluxes, Q, are defined negative into the ocean. DYNAMO = Dynamics of the MJO experiment; MJO = Madden-Julian Oscillation.

B_Q and B_R are compared in Figure 8. The value of B_R is often over an order of magnitude greater than the value of B_Q, yet instances of positive B_R are more episodic compared to the sinusoidal manner of positive B_Q.

Evaluation of (A5) with central Indian observations from Table A1 implies that the stabilizing rain-freshening multiplier on P, $S_0\beta$, is about 15 times the destabilizing rain-cooling multiplier on P, $\alpha\Delta T$, in (A5). This means that the stabilizing effect of rain freshening on surface buoyancy is 15 times larger than the destabilizing effect of rain cooling on surface buoyancy. Therefore, the effect of rain cooling on B and B_R can be ignored. B_R is always a positive, stabilizing flux, as shown in Figure 8 for the entire DYNAMO experiment.

The factor $\frac{\beta c_P}{\alpha L_V} S_0$ in (A6) is about 0.10 in the tropics using values from Table A1, so in regard to B and B_Q, the effect of evaporative cooling is overwhelmingly larger than the effect of evaporative salinification, which is also shown in Table A1 and by Asher et al. (2015).

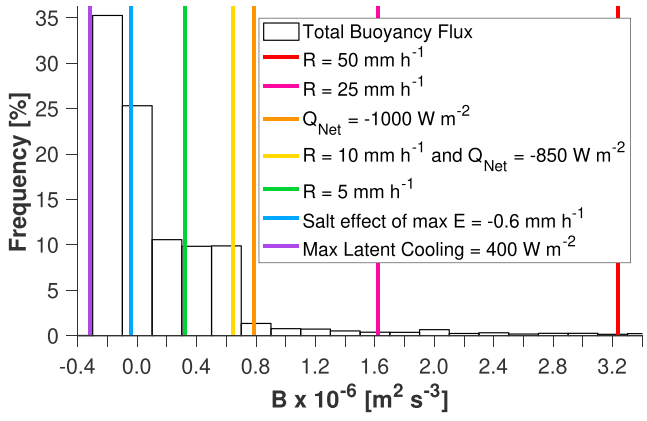

Figure A1. Normalized histogram of measured central Indian Ocean buoyancy flux, B. Vertical colored lines indicate B for various fluxes (negative fluxes = downward into ocean), rain rates, and evaporation.

Despite the fact that this study finds rain freshening to be responsible for greater B than solar heating (Figure 8), (A1) and (A6) actually overestimate the stabilizing effect of the net solar flux (Q_{Solar}) because, unlike the net longwave flux (Q_{IR}) that is absorbed within the top 100 μm, Q_{Solar} is not absorbed at the interface. Instead, roughly 50% of Q_{Solar} is absorbed within the top 0.5 m and the remainder is absorbed over the top 10 m (see Table 3 in Fairall, Bradley, Godfrey, et al., 1996; Soloviev & Lukas, 2006).

Appendix B: Processing of Precipitation Radar Data

The standard Yuter and Houze (1998) convective and stratiform radar echo partitioning algorithm was applied to the Z_h field at the lowest vertical level, which was at 0.75 km above sea level. The algorithm's tunable parameters were tested to produce the most physically realistic partitioning between convective and stratiform portions of storms in this data set (Houze, 1997; Schumacher et al., 2003; Steiner et al., 1995; Thompson et al., 2015; Yuter & Houze, 1998). Vertical cross sections of radar data were investigated during algorithm testing to ensure that stratiform rain classification was only made where a clear, robust radar bright band was occurring. Therefore, stratiform rain designations were only made when vertical profiles of radar data indicated that a melting layer and stratiform rain microphysical processes were both occurring. As part of the algorithm's standard procedures, background Z_h was smoothed about a 4 km radius of each grid point. The algorithm's climatological parameters were a = 60 and b = 100. First, grid points were classified as convective when Z_h exceed the smoothed background Z_h by 17 dBZ. Following standard procedures, neighboring grid points within 2, 3, 4, 5, and 6 km range from these convective grid points were also classified as convective if Z_h exceeded the following thresholds, respectively: 25, 25–30, 30–35, 35–40, and 40 dBZ.

In order to calculate R at each radar grid point, Z_h (dBZ) was first converted into linear units, z ($mm^6\ m^{-3}$) via: $z = 10^{(0.1Zh)}$. Then R was calculated at each grid point using two power law estimators, one for convective points: $R = 0.0366\ z^{0.684}$, and another for stratiform points: $R = 0.0258\ z^{0.644}$. These R estimators were developed by Thompson et al. (2015) for tropical oceanic rainfall experienced over the Indo-Pacific Warm Pool. If radar echo partitioning into convective and stratiform areas can be performed with confidence, using separate R estimators for convective and stratiform rain can significantly reduce error associated with R estimation (Thompson et al., 2015).

Acknowledgments

This research was the focus of a PhD dissertation at Colorado State University (CSU) Department of Atmospheric Science and was supported primarily by an interdisciplinary NSF Graduate Research Fellowship Award DGE-1321845 (E. J. T.) as well as NSF Award AGS-1063928 (S. A. R.) and NSF Award OCE-1059055 (J. N. M.). During the completion of this work, the first author (E. J. T.) was supported as a postdoctoral research associate at the Applied Physics Laboratory at the University of Washington (APL-UW). The oceanographic experimental support for this project was provided by ONR Award N0001-10-1-2098 (J. N. M.). C. W. Fairall's participation in DYNAMO was partially funded by the NOAA Climate Program Office's ESS division. Data access: http://data.eol.ucar.edu/master_list/?project=DYNAMO. We thank Paul Hein (CSU) for data management. We also thank the Ocean Mixing Group at Oregon State University (OSU) for collecting and providing all oceanographic data. We greatly appreciate conversations with Eric D. Maloney, Richard H. Johnson, David A. Randall, Charlotte A. DeMott, and Douglas C. Stolz (CSU), Aurélie Moulin and Simon de Szoeke (OSU), and William E. Asher, Kyla Drushka, and Eric A. D'Asaro (APL-UW). William E. Asher made substantial contributions in regard to manuscript editing and the synthesis of research results. Suggestions from two anonymous reviewers improved the manuscript and are gratefully acknowledged.

References

Anderson, J. E., & Riser, S. C. (2014). Near-surface variability of temperature and salinity in the near-tropical ocean: Observations from profiling floats. *Journal of Geophysical Research: Oceans*, *119*, 7433–7448. https://doi.org/10.1002/2014JC010112

Anderson, S. P., Weller, R. A., & Lukas, R. B. (1996). Surface buoyancy forcing and the mixed layer of the western Pacific warm pool: Observations and 1D model results. *Journal of Climate*, *9*(12), 3056–3085. https://doi.org/10.1175/1520-0442(1996)009<3056:SBFATM>2.0.CO;2

Asher, W. E., Jessup, A. T., Branch, R., & Clark, D. (2014). Observations of rain-induced near-surface salinity anomalies. *Journal of Geophysical Research: Oceans*, *119*, 5483–5500. https://doi.org/10.1002/2014JC009954

Asher, W. E., Jessup, A. T., & Clark, D. (2015). Stable near-surface ocean salinity stratifications due to evaporation observed during STRASSE. *Journal of Geophysical Research: Oceans*, *119*, 3219–3233. https://doi.org/10.1002/2014JC009808

Back, L. E., & Bretherton, C. S. (2009a). On the relationship between SST gradients, boundary layer winds, and convergence over the tropical oceans. *Journal of Climate*, *22*(15), 4182–4196. https://doi.org/10.1175/2009JCLI2392.1

Back, L. E., & Bretherton, C. S. (2009b). A simple model of climatological rainfall and vertical motion patterns over the tropical oceans. *Journal of Climate*, *22*(23), 6477–6497. https://doi.org/10.1175/2009JCLI2393.1

Barnes, H. C., & Houze, R. A. Jr. (2013). The precipitating cloud population of the Madden-Julian Oscillation over the Indian and west Pacific Oceans. *Journal of Geophysical Research: Atmospheres*, *118*, 6996–7023. https://doi.org/10.1002/jgrd.50375

Bellenger, H., & Duvel, J.-P. (2009). An analysis of tropical ocean diurnal warm layers. *Journal of Climate*, *22*(13), 3629–3646. https://doi.org/10.1175/2008JCLI2598.1

Bellenger, H., Takayabu, Y. N., Ushiyama, T., & Yoneyama, K. (2010). Role of diurnal warm layers in the diurnal cycle of convection over the tropical Indian Ocean during MISMO. *Monthly Weather Review*, *138*(6), 2426–2433. https://doi.org/10.1175/2010MWR3249.1

Benedict, J. J., & Randall, D. A. (2007). Observed characteristics of the MJO relative to maximum rainfall. *Journal of the Atmospheric Sciences*, *64*(7), 2332–2354. https://doi.org/10.1175/JAS3968.1

Bernie, D. J., Guilyardi, E., Madec, G., Slingo, J. M., Woolnough, S. J., & Cole, J. (2008). Impact of resolving the diurnal cycle in an ocean-atmosphere GCM. Part 2: A diurnally coupled CGCM. *Climate Dynamics*, *31*, 909–925. https://doi.org/10.1007/s00382-008-0429-z

Bernie, D. J., Guilyardi, E., Madec, G., Woolnough, S. J., & Slingo, J. M. (2007). Impact of resolving the diurnal cycle in an ocean-atmosphere GCM. Part 1: Diurnally forced OGCM. *Climate Dynamics*, *29*, 575–590. https://doi.org/10.1007/s00382-007-0249-6

Bernie, D. J., Woolnough, S. J., Slingo, J. M., & Guilyardi, E. (2005). Modeling diurnal and intraseasonal variability of the ocean mixed layer. *Journal of Climate*, *18*, 1190–1202. https://doi.org/10.1175/JCLI3319.1

Boutin, J., Martin, N., Reverdin, G., Yin, X., & Gaillard, F. (2013). Sea surface freshening inferred from SMOS and ARGO salinity: Impact of rain. *Ocean Science*, *9*(1), 183–192. https://doi.org/10.5194/os-9-183-2013

Brainerd, K. E., & Gregg, M. C. (1995). Surface mixed and mixing layer depths. *Deep-Sea Research Part I*, *42*(9), 1521–1543. https://doi.org/10.1016/0967-0637(95)00068-H

Brainerd, K. E., & Gregg, M. C. (1997). Turbulence and stratification on the tropical ocean-global atmosphere-coupled ocean-atmosphere response experiment microstructure pilot cruise. *Journal of Geophysical Research*, *102*, 10,437–10,455.

Carbone, R. E., & Li, Y. (2015). Tropical oceanic rainfall and sea surface temperature structure: Parsing causation from correlation in the MJO. *Journal of the Atmospheric Sciences*, *72*(7), 2703–2718. https://doi.org/10.1175/JAS-D-14-0226.1

Chen, S., Flatau, M., Jensen, T. G., Shinoda, T., Schmidt, J., May, P., et al. (2015). A study of CINDY/DYNAMO MJO suppressed phase. *Journal of the Atmospheric Sciences*, *72*(10), 3755–3779. https://doi.org/10.1175/JAS-D-13-0348.1

Chi, N.-H., Lien, R.-C., D'Asaro, E. A., & Ma, B. B. (2014). The surface mixed layer heat budget from mooring observations in the central Indian Ocean during Madden-Julian Oscillation events. *Journal of Geophysical Research: Oceans*, *119*, 4638–4652. https://doi.org/10.1002/2014JC010192

Clayson, C., & Bogdanoff, A. (2013). The effect of diurnal sea surface temperature warming on climatological air–sea fluxes. *Journal of Climate*, *26*(8), 2546–2556. https://doi.org/10.1175/JCLI-D-12-00062.1

Costa, A. A., Cotton, W. R., Walko, R. L., & Pielke, R. A. (2001). Coupled ocean-cloud-resolving simulations of the air-sea interaction over the equatorial western Pacific. *Journal of the Atmospheric Sciences*, *58*(22), 3357–3375. https://doi.org/10.1175/1520-0469(2001)058<3357:COCRSO>2.0.CO;2

Cronin, M. F., & McPhaden, M. J. (1999). Diurnal cycle of rainfall and surface salinity in the western Pacific warm pool. *Geophysical Research Letters*, *26*(23), 3465–3468. https://doi.org/10.1029/1999GL010504

Curry, J. A., Bentamy, A., Bourassa, M. A., Bourras, D., Bradley, E. F., Brunke, M., et al. (2004). SEAFLUX. *Bulletin of the American Meteorological Society*, *85*(3), 409–424. https://doi.org/10.1175/BAMS-85-3-409

D'Asaro, E., Black, P. G., Centurioni, L. R., Chang, Y., Chen, S. S., Foster, R. C., et al. (2014). Impact of Typhoons on the Ocean in the Pacific. *Bulletin of the American Meteorological Society*, *95*, 1405–1418. https://doi.org/10.1175/BAMS-D-12-00104.1

de Boyer Montégut, C., Madec, G., Fischer, A. S., Lazar, A., & Iudicone, D. (2004). Mixed layer depth over the global ocean: An examination of profile data and a profile-based climatology. *Journal of Geophysical Research*, *109*, C12003. https://doi.org/10.1029/2004JC002378

de Szoeke, S. P., Edson, J. B., Marion, J. R., Fairall, C. W., & Bariteau, L. (2014). The MJO and air-sea interaction in TOGA COARE and DYNAMO. *Journal of Climate*, *28*, 597–622.

de Szoeke, S. P., Skyllingstad, E. D., Zuidema, P., & Chandra, A. S. (2017). Cold pools and their influence on the tropical marine boundary layer. *Journal of the Atmospheric Sciences*, *74*(4), 1149–1168. https://doi.org/10.1175/JAS-D-16-0264.1

DeMott, C. A., Benedict, J. J., Klingaman, N. P., Woolnough, S. J., & Randall, D. A. (2016). Diagnosing ocean feedbacks to the MJO: SST-modulated surface fluxes and the moist static energy budget. *Journal of Geophysical Research: Atmospheres*, *121*, 8350–8373. https://doi.org/10.1002/2016JD025098

DeMott, C. A., Klingaman, N. P., & Woolnough, S. J. (2015). Atmosphere-ocean coupled processes in the Madden-Julian Oscillation. *Reviews of Geophysics*, *53*, 1099–1154. https://doi.org/10.1002/2014RG000478

DeMott, C. A., Stan, C., Randall, D. A., & Branson, M. D. (2014). Intraseasonal variability in coupled GCMs: The roles of ocean feedbacks and model physics. *Journal of Climate*, *27*(13), 4970–4995. https://doi.org/10.1175/JCLI-D-13-00760.1

Dorrestein, R. (1979). On the vertical buoyancy flux below the sea surface as induced by atmospheric factors. *Journal of Physical Oceanography*, *9*(1), 229–231. https://doi.org/10.1175/1520-0485(1979)009<0229:OTVBFB>2.0.CO;2

Drushka, K., Asher, W. E., Ward, B., & Walesby, K. (2016). Understanding the formation and evolution of rain-formed fresh lenses at the ocean surface. *Journal of Geophysical Research: Oceans*, *121*, 2673–2689. https://doi.org/10.1002/2015JC011527

Drushka, K., Sprintall, J., Gille, S. T., & Wijffels, S. (2012). In situ observations of Madden-Julian Oscillation mixed layer dynamics in the Indian and western Pacific oceans. *Journal of Climate*, *25*(7), 2306–2328. https://doi.org/10.1175/JCLI-D-11-00203.1

Edson, J. B., Jampana, V., Weller, R. A., Bigorre, S. P., Plueddemann, A. J., Fairall, C. W., et al. (2013). On the exchange of momentum over the open ocean. *Journal of Physical Oceanography*, *43*(8), 1589–1610. https://doi.org/10.1175/JPO-D-12-0173.1

Fairall, C. W., Bradley, E. F., Godfrey, J. S., Wick, G. A., Edson, J. B., & Young, G. S. (1996). Cool-skin and warm-layer effects on sea surface temperature. *Journal of Geophysical Research*, *101*(C1), 1295–1308. https://doi.org/10.1029/95JC03190

Fairall, C. W., Bradley, E. F., Hare, J. E., Grachev, A. A., & Edson, J. B. (2003). Bulk parameterization of air-sea fluxes: Updates and verification for the COARE algorithm. *Journal of Climate*, *16*(4), 571–591. https://doi.org/10.1175/1520-0442(2003)016<0571:BPOASF>2.0.CO;2

Fairall, C. W., Bradley, E. F., Rogers, D. P., Edson, J. B., & Young, G. S. (1996). Bulk parameterization of air-sea fluxes for Tropical Ocean- Global Atmosphere Coupled-Ocean Atmosphere Response Experiment. *Journal of Geophysical Research*, *101*(C2), 3747–3764. https://doi.org/10.1029/95JC03205

Fairall, C. W., Bradley, E. F., Godfrey, J. S., Wick, G. A., Edson, J. B., & Young, G. S. (1996). Cool-skin and warm-layer effects on sea surface temperature. *Journal of Geophysical Research*, *101*(C1), 1295–1308. https://doi.org/10.1029/95JC03190

Fairall, C. W., White, A. B., Edson, J. B., & Hare, J. E. (1997). Integrated shipboard measurements of the marine boundary layer. *Journal of Atmospheric and Oceanic Technology*, *14*(3), 338–359. https://doi.org/10.1175/1520-0426(1997)014<0338:ISMOTM>2.0.CO;2

Gosnell, R., Fairall, C. W., & Webster, P. J. (1995). The sensible heat of rainfall in the tropical ocean. *Journal of Geophysical Research*, *100*, 18,437–18,442.

Gottschalck, J., Roundy, P. E., Schreck, C. J. III, Vintzileos, A., & Zhang, C. (2013). Large-scale atmospheric and oceanic conditions during the 2011-2012 DYNAMO field campaign. *Monthly Weather Review*, *141*(12), 4173–4196. https://doi.org/10.1175/MWR-D-13-00022.1

Gould, W. J., & Turton, J. (2006). Argo -Sounding the oceans. *Weather*, *61*, 17–21. https://doi.org/10.1256/wea.56.05

Harrison, D. E., & Vecchi, G. A. (1997). Westerly wind events in the tropical Pacific, 1986–95. *Journal of Climate*, *10*(12), 3131–3156. https://doi.org/10.1175/1520-0442(1997)010<3131:WWEITT>2.0.CO;2

Holte, J., Talley, L. D., Gilson, J., & Roemmich, D. (2017). An Argo mixed layer climatology and database. *Geophysical Research Letters*, *44*, 5618–5626. https://doi.org/10.1002/2017GL073426

Houze, R. A. Jr. (1997). Stratiform precipitation in regions of convection: A meteorological paradox? *Bulletin of the American Meteorological Society*, *78*(10), 2179–2196. https://doi.org/10.1175/1520-0477(1997)078<2179:SPIROC>2.0.CO;2

Houze, R. A. Jr., Rasmussen, K. L., Zuluaga, M. D., & Brodzik, S. R. (2015). The variable nature of convection in the tropics and subtropics: A legacy of 16 years of the Tropical Rainfall Measuring Mission satellite. *Reviews of Geophysics*, *53*, 994–1021. https://doi.org/10.1002/2015RG000488

Hung, M., Lin, J., Wang, W., Kim, D., Shinoda, T., & Weaver, S. J. (2013). MJO and convectively coupled equatorial waves simulated by CMIP5 climate models. *Journal of Climate*, *26*, 6185–6214. https://doi.org/10.1175/JCLI-D-12-00541.1

Johnson, R., & Ciesielski, P. (2013). Structure and properties of Madden-Julian Oscillations deduced from DYNAMO sounding arrays. *Journal of the Atmospheric Sciences*, *70*(10), 3157–3179. https://doi.org/10.1175/JAS-D-13-065.1

Johnson, R. H., & Ciesielski, P. E. (2017). Multiscale variability of the atmospheric boundary layer during DYNAMO. *Journal of the Atmospheric Sciences*, *74*, 4003–4021. https://doi.org/10.1175/JAS-D-17-0182.1

Johnson, R. H., Rickenbach, T. M., Rutledge, S. A., Ciesielski, P. E., & Schubert, W. H. (1999). Trimodal characteristics of tropical convection. *Journal of Climate*, *12*(8), 2397–2418. https://doi.org/10.1175/1520-0442(1999)012<2397:TCOTC>2.0.CO;2

Jourdain, N. C., Lengaigne, M., Vialard, J., Madec, G., Menkes, C. E., Vincent, E. M., et al. (2013). Observation-based estimates of surface cooling inhibition by heavy rainfall under tropical cyclones. *Journal of Physical Oceanography*, *43*, 205–221. https://doi.org/10.1175/JPO-D-12-085.1

Kawai, Y., & Wada, A. (2007). Diurnal sea surface temperature variation and its impact on the atmosphere and ocean: A review. *Oceanography*, *63*(5), 721–744. https://doi.org/10.1007/s10872-007-0063-0

Kilpatrick, T., & Xie, S.-P. (2015). ASCAT observations of downdrafts from mesoscale convective systems. *Geophysical Research Letters*, *42*, 1951–1958. https://doi.org/10.1002/2015GL063025

Kilpatrick, T., & Xie, S.-P. (2016). Circumventing rain-related errors in scatterometer wind observations. *Journal of Geophysical Research: Atmospheres*, *121*, 9422–9440. https://doi.org/10.1002/2016JD025105

Klingaman, N. P., & Woolnough, S. J. (2014). The role of air-sea coupling in the simulation of the Madden-Julian Oscillation in the Hadley Centre model. *Quarterly Journal of the Royal Meteorological Society*, *140*(684), 2272–2286. https://doi.org/10.1002/qj.2295

Klingaman, N. P., Woolnough, S. J., Weller, H., & Slingo, J. M. (2011). The impact of finer-resolution air-sea coupling on the intraseasonal oscillation of the Indian summer monsoon. *Journal of Climate*, *24*(10), 2451–2468. https://doi.org/10.1175/2010JCLI3868.1

Kummerow, C., Barnes, W., Kozu, T., Shiue, J., & Simpson, J. (1998). The Tropical Rainfall Measuring Mission (TRMM) sensor package. *Journal of Atmospheric and Oceanic Technology*, *15*, 809–817. https://doi.org/10.1175/1520-0426(1998)015<0809:TTRMMT>2.0.CO;2

Lau, W. K. M., & Waliser, D. E. (2005). *Intraseasonal variability of the atmosphere-ocean climate system* (p. 474). Heidelberg, Germany: Springer.

Li, Y., & Carbone, R. E. (2012). Excitation of rainfall over the tropical western Pacific. *Journal of the Atmospheric Sciences*, *69*, 2983–2994.

Lin, J., Kiladis, G. N., Mapes, B. E., Weickmann, K. M., Sperber, K. R., Lin, W., et al. (2006). Tropical intraseasonal variability in 14 IPCC AR4 climate models. Part I: Convective signals. *Journal of Climate*, *19*, 2665–2690. https://doi.org/10.1175/JCLI3735.1

Lindzen, R., & Nigam, S. (1987). On the role of sea surface temperature gradients in forcing low level winds and convergence in the tropics. *Journal of the Atmospheric Sciences*, *44*, 2418–2436.

Lombardo, C. P., & Gregg, M. C. (1989). Similarity scaling of viscous and thermal dissipation in a convecting surface boundary layer. *Journal of Geophysical Research*, *94*(C5), 6273–6284. https://doi.org/10.1029/JC094iC05p06273

Lukas, R., & Lindstrom, E. (1991). The mixed layer of the western equatorial Pacific Ocean. *Journal of Geophysical Research*, *96*(S01), 3343–3335. https://doi.org/10.1029/90JC01951

Matthews, A. J., Baranowski, D. B., Heywood, K. J., Flatau, P. J., & Schmidtko, S. (2014). The surface diurnal warm layer in the Indian Ocean during CINDY/DYNAMO. *Journal of Climate*, *27*, 1658–1672.

McDougall, T. J., & Barker, P. M. (2011). Getting started with TEOS-10 and the Gibbs Seawater (GSW) Oceanographic Toolbox (28 pp.). SCOR/IAPSO WG127.

Miller, J. (1976). The salinity effect in a mixed layer ocean model. *Journal of Physical Oceanography*, *6*(1), 29–35. https://doi.org/10.1175/1520-0485(1976)006<0029:TSEIAM>2.0.CO;2

Moulin, A. J., Moum, J. N., & Shroyer, E. L. (2018). Evolution of turbulence in the diurnal warm layer. *Journal of Physical Oceanography*, *48*(2), 383–396. https://doi.org/10.1175/JPO-D-17-0170.1

Moum, J. N., de Szoeke, S. P., Smyth, W. D., Edson, J. B., DeWitt, H. L., Moulin, A. J., et al. (2014). Air-sea interactions from MJO westerly wind bursts. *Bulletin of the American Meteorological Society*, *95*(8), 1185–1199. https://doi.org/10.1175/BAMS-D-12-00225.1

Moum, J. N., Gregg, M. C., Lien, R. C., & Carr, M. E. (1995). Comparison of turbulent kinetic energy dissipation rates from two ocean microstructure profilers. *Journal of Atmospheric and Oceanic Technology*, *12*(2), 346–366. https://doi.org/10.1175/1520-0426(1995)012<0346:COTKED>2.0.CO;2

Pendergrass, A. G., & Deser, C. (2017). Climatological characteristics of typical daily precipitation. *Journal of Climate*, *30*(15), 5985–6003. https://doi.org/10.1175/JCLI-D-16-0684.1

Praveen Kumar, B., Vialard, J., Lengaigne, M., Murty, V. S. N., & McPhaden, M. J. (2012). TropFlux: Air-sea fluxes for the global tropical oceans—Description and evaluation. *Climate Dynamics*, *38*(7-8), 1521–1543. https://doi.org/10.1007/s00382-011-1115-0

Price, J. F. (1979). Observations of a rain-formed mixed layer. *Journal of Physical Oceanography*, *9*(3), 643–649. https://doi.org/10.1175/1520-0485(1979)009<0643:OOARFM>2.0.CO;2

Price, J. F., Weller, R. A., & Pinkel, R. (1986). Diurnal cycling: Observations and models of the upper ocean response to diurnal heating, cooling, and wind mixing. *Journal of Geophysical Research*, *91*(C7), 8411–8427. https://doi.org/10.1029/JC091iC07p08411

Prytherch, J., Farrar, J. T., & Weller, R. A. (2013). Moored surface buoy observations of the diurnal warm layer. *Journal of Geophysical Research: Oceans*, *118*, 4553–4569. https://doi.org/10.1002/jgrc.20360

Pujiana, K., Moum, J. N., & Smyth, W. D. (2018). The role of turbulence in redistributing upper-ocean heat, freshwater, and momentum in response to the MJO in the equatorial Indian Ocean. *Journal of Physical Oceanography*, *48*, 197–220. https://doi.org/10.1175/JPO-D-17-0146.1

Reverdin, G., Morisset, S., Boutin, J., & Martin, N. (2012). Rain-induced variability of near sea-surface T and S from drifter data. *Journal of Geophysical Research*, *117*, C02032. https://doi.org/10.1029/2011JC007549

Rickenbach, T. M., & Rutledge, S. A. (1998). Convection in TOGA COARE: Horizontal scale, morphology, and rainfall production. *Journal of the Atmospheric Sciences*, *55*, 2715–2729. https://doi.org/10.1175/1520-0469(1998)055<2715:CITCHS>2.0.CO;2

Riley, E. M., Mapes, B. E., & Tulich, S. N. (2011). Clouds associated with the Madden-Julian Oscillation: A new perspective from CloudSat. *Journal of the Atmospheric Sciences*, *68*, 3032–3051. https://doi.org/10.1175/JAS-D-11-030.1

Rowe, A. K., & Houze, R. A. Jr. (2015). Cloud organization and growth during the transition from suppressed to active MJO conditions. *Journal of Geophysical Research: Atmospheres*, *120*, 10,324–10,350. https://doi.org/10.1002/2014JD022948

Ruppert, J. H. (2016). Diurnal timescale feedbacks in the tropical cumulus regime. *Journal of Advances in Modeling Earth Systems*, *8*, 1483–1500. https://doi.org/10.1002/ 2016MS000713

Ruppert, J. H., & Johnson, R. H. (2015). Diurnally modulated cumulus moistening in the pre-onset stage of the Madden-Julian Oscillation during DYNAMO. *Journal of the Atmospheric Sciences*, *72*(4), 1622–1647. https://doi.org/10.1175/JAS-D-14-0218.1

Ruppert, J. H. Jr., & Johnson, R. H. (2016). On the cumulus diurnal cycle over the tropical warm pool. *Journal of Advances in Modeling Earth Systems*, *8*, 669–690. https://doi.org/10.1002/2015MS000610

Sakaeda, N., Powell, S. W., Dias, J., & Kiladis, G. N. (2018). The diurnal variability of precipitating cloud populations during DYNAMO. *Journal of the Atmospheric Sciences*, *75*(4), 1307–1326. https://doi.org/10.1175/JAS-D-17-0312.1

Santos-Garcia, A., Jacob, M. M., Jones, W. L., Asher, W. E., Hejazin, Y., Ebrahimi, H., & Rabolli, M. (2014). Investigation of rain effects on Aquarius sea surface salinity measurements. *Journal of Geophysical Research: Oceans*, *119*, 7605–7624. https://doi.org/10.1002/2014JC010137

Schmidtko, S., Johnson, G. C., & Lyman, J. M. (2013). A global monthly isopycnal upper-ocean climatology with mixed layers. *Journal of Geophysical Research: Oceans*, *118*, 1658–1672. https://doi.org/10.1002/jgrc.20122

Seo, H., Subramanian, A. C., Miller, A. J., & Cavanaugh, N. R. (2014). Coupled impacts of the diurnal cycle of sea surface temperature on the Madden-Julian Oscillation. *Journal of Climate*, *27*(22), 8422–8443. https://doi.org/10.1175/JCLI-D-14-00141.1

Shinoda, T., & Hendon, H. H. (1998). Mixed layer modeling of intraseasonal variability in the tropical Western Pacific and Indian Oceans. *Journal of Climate*, *11*, 2668–2685. https://doi.org/10.1175/1520-0442(1998)011<2668:MLMOIV>2.0.CO;2

Smyth, W. D., Hebert, D., & Moum, J. N. (1996a). Local ocean response to a multiphase westerly wind burst: 1. Dynamic response. *Journal of Geophysical Research*, *101*, 22,495–22,512.

Smyth, W. D., Hebert, D., & Moum, J. N. (1996b). Local ocean response to a multiphase westerly wind burst: 2. Thermal and freshwater responses. *Journal of Geophysical Research*, *101*, 22,513–22,533.

Soloviev, A., & Lukas, R. (1996). Observation of spatial variability of diurnal thermocline and rain-formed halocline in the western Pacific warm pool. *Journal of Physical Oceanography*, *26*, 2529–2538. https://doi.org/10.1175/1520-0485(1996)026<2529:OOSVOD>2.0.CO;2

Soloviev, A., & Lukas, R. (1997). Sharp frontal interfaces in the near-surface layer of the Ocean in the Western Equatorial Pacific warm pool. *Journal of Physical Oceanography*, *27*, 999–1017. https://doi.org/10.1175/1520-0485(1997)027<0999:SFIITN>2.0.CO;2

Soloviev, A., & Lukas, R. (2006). *The near-surface layer of the ocean: Structure, dynamics and applications* (p. 574). Netherlands: Springer.

Soloviev, A., Matt, S., & Fujimura, A. (2015). Three-dimensional dynamics of fresh water lenses in the ocean's near-surface layer. *Oceanography*, *28*(1), 142–149. https://doi.org/10.5670/oceanog.2015.14

Soloviev, A., & Vershinsky, N. (1982). The vertical structure of the thin surface layer of the ocean under conditions of low wind speed. *Deep Sea Research*, *29*(12), 1437–1449. https://doi.org/10.1016/0198-0149(82)90035-8

Stan, C., Khairoutdinov, M., DeMott, C. A., Krishnamurthy, V., Straus, D. M., Randall, D. A., et al. (2010). An ocean-atmosphere climate simulation with an embedded cloud resolving model. *Geophysical Research Letters*, *37*, L01702. https://doi.org/10.1029/2009GL040822

Stuart-Menteth, A. C., Robinson, I. S., & Challenor, P. G. (2003). A global study of diurnal warming using satellite-derived sea surface temperature. *Journal of Geophysical Research*, *108*(C5), 3155. https://doi.org/10.1029/2002JC001534

Thompson, E. J., Rutledge, S. A., Dolan, B., & Thurai, M. (2015). Drop size distributions and radar observations of convective and stratiform rain over the equatorial Indian and west Pacific Oceans. *Journal of the Atmospheric Sciences*, *72*(11), 4091–4125. https://doi.org/10.1175/JAS-D-14-0206.1

Webster, P. J., Clayson, C. A., & Curry, J. A. (1996). Clouds, radiation, and the diurnal cycle of sea surface temperature in the tropical western Pacific. *Journal of Climate*, *9*(8), 1712–1730. https://doi.org/10.1175/1520-0442(1996)009<1712:CRATDC>2.0.CO;2

Wheeler, M. C., & Hendon, H. H. (2004). An all-season real-time multivariate MJO index: Development of an index for monitoring and prediction. *Monthly Weather Review*, *132*(8), 1917–1932. https://doi.org/10.1175/1520-0493(2004)132<1917:AARMMI>2.0.CO;2

Wijesekera, H. W., & Gregg, M. C. (1996). Surface layer response to weak winds, westerly bursts, and rain squalls in the western Pacific warm pool. *Journal of Geophysical Research*, *101*(C1), 977–997. https://doi.org/10.1029/95JC02553

Wijesekera, H. W., Paulson, C. A., & Huyer, A. (1999). The effect of rainfall on the surface layer during a westerly wind burst in the western equatorial Pacific. *Journal of Geophysical Research*, *29*, 612–632.

Woolnough, S. J., Slingo, J. M., & Hoskins, B. J. (2000). The relationship between convection and sea surface temperature on intraseasonal timescales. *Journal of Climate*, *13*(12), 2086–2104. https://doi.org/10.1175/1520-0442(2000)013<2086:TRBCAS>2.0.CO;2

Woolnough, S. J., Slingo, J. M., & Hoskins, B. J. (2001). The organization of tropical convection by intraseasonal sea surface temperature anomalies. *Quarterly Journal of the Royal Meteorological Society*, *127*(573), 887–907. https://doi.org/10.1002/qj.49712757310

Xu, W., & Rutledge, S. A. (2014). Convective characteristics of the Madden-Julian Oscillation over the central Indian Ocean observed by shipborne radar during DYNAMO. *Journal of the Atmospheric Sciences*, *71*(8), 2859–2877. https://doi.org/10.1175/JAS-D-13-0372.1

Xu, W., & Rutledge, S. A. (2015). Morphology, intensity, and rainfall production of MJO convection: Observations from DYNAMO and TRMM. *Journal of the Atmospheric Sciences*, *72*(2), 623–640. https://doi.org/10.1175/JAS-D-14-0130.1

Yang, G.-Y., & Slingo, J. (2001). The diurnal cycle in the tropic. *Monthly Weather Review*, *129*(4), 784–801. https://doi.org/10.1175/1520-0493(2001)129<0784:TDCITT>2.0.CO;2

Yoneyama, K., Zhang, C., & Long, C. N. (2013). Tracking pulses of the Madden-Julian Oscillation. *Bulletin of the American Meteorological Society*, *94*(12), 1871–1891. https://doi.org/10.1175/BAMS-D-12-00157.1

You, Y. (1995). Salinity variability and its role in the barrier-layer formation during TOGA-COARE. *Journal of Physical Oceanography*, *25*, 2778–2807.

Yuter, S., & Houze, R. A. Jr. (1998). The natural variability of precipitating clouds over the western Pacific warm pool. *Quarterly Journal of the Royal Meteorological Society*, *124*(545), 53–99. https://doi.org/10.1002/qj.49712454504

Zhang, C. (2005). Madden-Julian Oscillation. *Reviews of Geophysics*, *43*, RG2003. https://doi.org/10.1029/2004RG000158

Zhang, C. (2013). Madden–Julian Oscillation: Bridging weather and climate. *Bulletin of the American Meteorological Society*, *94*(12), 1849–1870. https://doi.org/10.1175/BAMS-D-12-00026.1